Applied Catalysis B: Environmental 291 (2021) 119797

Contents lists available at ScienceDirect

Applied Catalysis B: Environmental

journal homepage: www.elsevier.com/locate/apcatb

Hydrogenation and C—S bond activation pathways in thiophene and tetrahydrothiophene reactions on sulfur-passivated surfaces of Ru, Pt, and Re nanoparticles

Edwin Yik [a,b], David Hibbitts [c], Huamin Wang [a,d], Enrique Iglesia [a,e,*]

[a] Department of Chemical and Biomolecular Engineering, University of California, Berkeley, CA, 94720, USA
[b] Current: 4550 N. Park Ave., Chevy Chase, MD, 20815, USA
[c] Department of Chemical Engineering, University of Florida, Gainesville, FL, 32611, USA
[d] Current: Energy Processes & Materials Division, Pacific Northwest National Laboratory, Richland, WA, 99352, USA
[e] Physical Sciences Division, Pacific Northwest National Laboratory, Richland, WA, 99352, USA

ARTICLE INFO

This article is dedicated to the memory of Maria Flytzani-Stephanopoulos in remembrance and recognition of her contributions to the science and practice of catalysis, her role as editor, teacher and mentor, and her dedication to service.

Keywords:
Re
Ru
Pt
Transition metals
Thiophene hydrodesulfurization
C-S bond activation
C-S bond scission
Hydrogenation
Hydrogenolysis
Heteroatoms

ABSTRACT

Thiophene-H_2 reactions proceed via sulfur removal and hydrogenation routes on dispersed metal nanoparticles that become decorated by refractory S adlayers during catalysis. The identity and kinetic relevance of the required elementary steps are described here based on rates measured at S-chemical potentials set by H_2S/H_2 ratios similar to those prevalent during practical catalysis on Re, ReS_x, Ru, and Pt catalysts. The free energies of formation of S adatoms from H_2S/H_2 reactants are large and negative at low coverages (< -50 kJ mol^{-1} on Pt (111) and < -150 kJ mol^{-1} on Re(0001) and Ru(0001)), but strong repulsion among adatoms prevents full saturation, leading to sub-monolayer coverages and to passivated surfaces that expose uncovered interstices. The residual interstitial spaces (*) within adlayers of unreactive S-atoms (S′) bind intermediates and transition states reversibly, thus allowing these passivated surfaces to carry out catalytic turnovers. These interstices are larger on Pt than on Ru or Re surfaces, leading to concomitantly higher turnover rates for thiophene hydrogenation and desulfurization routes. The identity and kinetic relevance of elementary steps for desulfurization (to form C_4 hydrocarbons) and hydrogenation (to form tetrahydrothiophene; THT) are similar among these catalysts; they involve kinetically-relevant H-addition steps of thiophene-derived intermediates that cleave their C—S bonds or "over-hydrogenate" to THT in one surface sojourn. THT undergoes C—S bond cleavage in secondary reactions that correct this over-hydrogenation to form the more unsaturated species that cleave C—S bonds. THT/C_4 product ratios are insensitive to H_2S/H_2 ratios and thiophene pressure, even though active interstitial spaces are covered by kinetically-detectable S* and bound thiophene; therefore, primary and secondary reactions must occur on the same active ensembles. The observed increase in THT/C_4 ratios with H_2 pressure shows that THT formation transition states involve a larger number of H-atoms than for C—S cleavage. C—S bonds cleave in species with partial unsaturation (H-contents between those in THT and thiophene), in processes that are reminiscent of the requirement to add or remove H-atoms from C and O atoms in cleaving C—C and C—O bonds in alkanes and alkanols, as well as C—O bonds in CO hydrogenation reactions. The rate and selectivity data and the mechanistic conclusions described here show that thiophene hydrogenation and desulfurization routes require similar binding interstices within refractory S adlayers and that metal-sulfur bond energies act as indirect descriptors of reactivity because they determine the number, size, and binding properties of the exposed weakly-binding ensembles that stabilize the relevant transition states and enable catalytic turnovers.

1. Introduction

The presence of organosulfur compounds in reactant streams imposes significant hurdles in the processing and marketing of chemicals and fuels because of their toxic effects on humans and catalyst binding sites, as well as their tendency to form SO_x as combustion products. Their removal via hydrodesulfurization (HDS) typically requires high H_2 pressures for hydrogenative cleavage of C—S bonds. Many mechanistic

* Corresponding author at: Department of Chemical and Biomolecular Engineering, University of California, Berkeley, CA, 94720, USA.
E-mail address: iglesia@berkeley.edu (E. Iglesia).

https://doi.org/10.1016/j.apcatb.2020.119797
Received 9 September 2020; Received in revised form 17 November 2020; Accepted 21 November 2020
Available online 9 December 2020
0926-3373/

proposals for such reactions rely on kinetic data for S-removal on multicomponent catalysts relevant to practice but of complex morphology (such as supported and unsupported Co(Ni)-Mo(W) sulfides) [1–4] in three-phase reactors at conditions and conversions that preclude strict kinetic control or rigorous mechanistic inquiries.

HDS reactions are catalyzed by diverse compositions of metal and sulfide nanoparticles [5–14]; comparisons among these catalysts, however, often assume that they retain their initial sulfide or metal phases and stoichiometry upon exposure to the sulfur chemical potentials prevalent during use. These assumptions have led to the counting of "active sites" from uptakes of titrants that are purported to bind selectively at such sites. These titrants bind instead at sulfur vacancies formed by reductive treatments at conditions prescribed for such titrations, chosen arbitrarily and very different from those prevalent during HDS reactions. These uptakes (e.g., O_2 on Co-MoS_x phases after treatment in H_2 [5]) reflect an occasionally useful combination of the total number of binding sites and the reducibility of their surface M–S species. As a result, they often correlate by coincidence with HDS rates, but they do not represent the number of active sites. Consequently, they do not give turnover rates, when used to normalize rates, which reflect inherent reactivity differences among catalysts. Structure-function relations based on such "turnover rates" have emerged [5,7,13], without evidence that the elementary steps and their kinetic relevance are even the same among very disparate compositions.

Our previous studies of thiophene HDS on well-defined SiO_2-supported monometallic Ru [8], Pt [9], and Re [15] nanoparticles showed that nanoparticle surfaces contain refractory templates of irreversibly-bound S adatoms (S′) at the sulfur chemical potentials that prevail during HDS practice (10^{-5}–10^{-2} H_2S/H_2 ratios, 573−623 K). These refractory adlayers represent the mechanism by which H_2S and organosulfur compounds strongly inhibit (de)hydrogenation, hydrogenolysis, and reforming reactions, even at very high H_2 pressures and low H_2S/H_2 ratios. These refractory templates retain reactive interstices, on which turnovers can still occur through the reversible adsorption-desorption of reactants and products. These adlayers weaken the binding of intermediates through repulsive S–S interactions; as a result, they passivate such surfaces from self-poisoning by strongly-bound species derived from HDS reactants and products.

The number, size, and binding properties of such interstices can vary significantly among catalyst systems, as evident even for a given element when it is present in its metal (Re) or sulfide (ReS_x) forms [15]. Their kinetic and selectivity trends are similar, but rates are more than 100-fold greater on ReS_x than on Re metal. The interstitial sites on these two catalysts differ not in their intrinsic mechanism but in their number and binding properties for the relevant transition states [15]. The surface of Re nanoparticles stabilizes denser S′ adlayers than on ReS_x, merely because M—S′ bonds are much stronger on Re than on ReS_x surfaces. The intrinsic properties of catalytic nanoparticle surfaces are dictated by the structure and composition of their bulk phase and thus determine the surface density of active interstices and account, in addition to any differences in the free energy of activation on such ensembles, for the differences in measured rates.

This study addresses thiophene reaction rates and kinetic rate equations determined under conditions of strict kinetic control. These data reveal that thiophene reactions on Ru and Pt surfaces occur on interstitial spaces, present within an essentially inert adlayer composed of refractory "spectator" S′ species, that stabilize C—S bond cleavage and hydrogenation transition states, as in the case of Re and ReS_x catalysts [15]. Previous studies on Ru [8] and Pt [9] did not properly take into account the extent of fast secondary tetrahydrothiophene (THT) desulfurization in assessing the primary routes to thiophene products, thus inaccurately concluding that sulfur coverages, set by H_2S/H_2 ratios, influence the relative rates of primary desulfurization and hydrogenation routes [8,9,16,17]; the observed selectivity trends with residence time instead reflect the lower prevalent conversions at higher H_2S/H_2 ratios, which lead to imperfect extrapolations to the conditions at the bed inlet and to seemingly higher primary THT selectivities [15].

HDS reactions on Ru, Pt, and Re/ReS_x [15] catalysts involve similar elementary steps. They include a kinetically-relevant H-addition step that limits the rate at which thiophene is consumed to form bound intermediates common to the formation of THT (hydrogenation route) and butene/butane (C_4, "direct" desulfurization route) products. Both routes involve the same active sites and intermediates and sense the occupancy of the binding centers by coadsorbed species to similar extents. THT products are favored at higher H_2 pressures because their associated transition states contain a larger number of H-atoms than for C_4 formation. THT readsorbs onto the binding sites from which it desorbs, thus allowing subsequent sojourns that can cleave the C—S bond via dehydrogenation events that merely reverse the H-addition steps that formed it. C—S bond cleavage is mediated by transition states consisting of partially-hydrogenated thiophene species; C—S bonds are weakened by multiple C and S bonds to surfaces, made possible by fewer C—H bonds. Such unsaturation is also required in alkane and alkanol hydrogenolysis reactions that cleave C—C and C—O bonds, respectively [18–21]. These C—S cleavage transition states benefit entropically from the fewer number of H_2 molecules required to form them from thiophene compared with those required to form THT.

Turnover rates (per exposed metal atom) on Re, Ru, and Pt nanoparticles differ significantly, indicative of very different binding properties for bound intermediates and transition states at interstitial ensembles within dense S′ adlayers on their surfaces, which contain M—S′ bonds of different strengths. Such differences are evident from M—S bond energies derived from theory, which allow estimates of S′ coverages at different sulfur chemical potentials (set by H_2S/H_2 ratios); these S′ coverages, however, vary less than two-fold among surfaces that differ in areal thiophene conversion nearly 100-fold. Such observations indicate that transition states sense the working surfaces quite differently than S-atoms, in both their binding and in the requisite spatial requirements for the interstitial ensembles. The widely reported relationships between reactivity and M—S bond energy thus reflect a fortuitous outcome of how both the concentration and transition state binding of these interstitial spaces are influenced, in a predictable manner, by the M—S bond strength of the underlying substrate.

2. Methods

The protocols for the synthesis of nearly monodispersed clusters of Ru [8], Pt [9], and Re [15], the details of their characterization, and the procedures used to ensure that rate measurements were carried out under conditions of strict kinetic control have been reported previously [8,9,15] and are summarized briefly below. The methods used to examine sulfur adsorption on close-packed surfaces of Ru, Pt, and Re using density functional theory (DFT) are also provided.

2.1. Catalyst synthesis procedures

Metal nanoparticles (1.6–6.9 nm) were prepared on inert SiO_2 supports (Cabosil, HS-5, 310 $m^2\ g^{-1}$) that were previously acid-washed and treated in dry air at 673−773 K (0.003 K s^{-1}) for 3−4 h. Basic aqueous solutions of $Ru(NH_3)_6Cl_3$ (Aldrich, 98 %) or $Pt(NH_3)_4(NO_3)_2$ (Alfa Aesar, 99.99 %) were mixed with SiO_2 (200 $cm^3\ g^{-1}$ SiO_2) and stirred for 1 h in the presence of additional NaOH (EMD Chemicals Inc.) or $NH_3{\cdot}H_2O$, respectively (final pH 11.2 and 9.2, respectively), at ambient temperature. The solids were then filtered, and in the case of Ru, rinsed thoroughly with deionized water (17.9 M·Ω resistivity) and filtered in order to remove traces of residual chloride ions. The recovered solids were treated in vacuum for >24 h at ambient temperature and then in flowing dry air (Praxair, 99.99 %, 1.0 $cm^3\ g^{-1}\ s^{-1}$) at 353−373 K for 5 h.

Re nanoparticles and ReS_x nanostructures were prepared by dropwise introduction of aqueous NH_4ReO_4 solutions (Aldrich 99 %+) into SiO_2 powders to the point of incipient wetness. This process was repeated with intervening drying steps in stagnant air at 353 K for >12 h

in order to reach the target Re contents, a process that was required because of the low solubility of NH_4ReO_4 in water. After impregnation, samples were treated in vacuum for >12 h at ambient temperature and then in flowing dry air at 353 K for >12 h.

All samples (Ru, Pt, Re) were then treated in dry air and then in H_2 in order to obtain nanoparticles with different diameters [8,9,15] or in H_2S/He (after loading in a packed bed reactor) to obtain ReS_x phases. All samples were passivated before exposure to ambient air by treatment in 0.1–0.5 % O_2/He (Praxair) flow for 2−6 h at ambient temperature. Table 1 lists the samples referenced in this study, together with the specific thermal treatments used in their respective synthesis protocols.

2.2. Catalyst characterization

Nominal metal contents, reported in Table 1, were confirmed (within 10 %) by inductively-coupled plasma optical emission spectroscopy (ICP-OES, Galbraith Laboratories, Inc.). The dispersion of the metal nanoparticles was measured from chemisorption uptakes of H_2 (at 313 K for Ru, Pt) and of O_2 (at 323 K for Re) on samples treated in H_2 (673−773 K) and then evacuated for 1 h. Isotherms were collected over a range of H_2 and O_2 pressures (1−120 kPa) that led to saturation coverages of strongly-bound titrants. Dispersions were calculated by assuming surface stoichiometries of 1:1 H/Ru_s, 1:1 H/Pt_s, and 0.4:1 O/Re_s; the O/Re_s stoichiometry was determined from O_2 surface-saturation uptake measurements and surface-averaged particle sizes from transmission electron microscopy (TEM) [15]. Dispersions from chemisorption data were used to estimate mean diameters by assuming hemispherical nanoparticles and the bulk density of each metal.

Samples were dispersed onto lacey carbon films supported on 400 mesh copper grids (Ted Pella, Inc.) for transmission electron microscopy analysis (TEM; JEOL 1200 EX at 80 kV or Philips 420 at 120 kV). Size distributions were obtained by imaging >300 Ru and Re nanoparticles. These distributions were used to estimate surface-averaged diameters:

$$\frac{\Sigma_i\, n_i d_i^3}{\Sigma_i\, n_i d_i^2} \quad (1)$$

where n_i is the number of nanoparticles with diameter d_i. The similar diameters derived from TEM and chemisorption uptakes are indicative of clean and fully accessible nanoparticle surfaces [8,15]. For Re samples treated in H_2S/He, layered structures typical of ReS_2 morphologies reported [22] were observed in TEM without any evidence of isotropic nanoparticles [15].

Temperature-programmed reduction measurements in H_2 (TPR) and X-ray absorption spectra (XAS, SSRL, beamline 4-1) were used to determine the prevalent phases in fresh samples and after these samples were exposed to sulfur chemical potentials and conditions (3.0 MPa H_2, 3.0 kPa H_2S, 573−623 K) similar to those of HDS reactions (denoted as spent samples). Sulfur-to-metal (S/M) ratios in spent samples were determined by monitoring H_2S evolution during TPR using mass spectrometry (Leybold Inficon, Transpector Series) with response factors obtained from H_2S/H_2/He mixtures of known composition; S/M ratios below unity were observed for Ru/SiO_2 and Re/SiO_2 [8,15], indicating that sulfidation upon contact with H_2S/H_2 mixtures was restricted to nanoparticle surfaces, with the bulk retaining its initial zero-valent phase. For Re samples treated in H_2S/He, S/M ratios measured in fresh and spent samples were larger than unity (2.1 and 1.3, respectively), indicative of bulk sulfidation [15]. X-ray absorption fine structure of fresh and spent samples confirmed the retention of the zero-valent (Ru, Re) bulk phase and the retention of Re sulfide bulk phase in ReS_x samples [8,15].

2.3. Measurements of thiophene conversion rates and selectivities

Passivated catalysts were diluted with acid-washed and air-treated SiO_2 (Cab-O-Sil, HS-5; SiO_2:catalyst = 1−9 wt.:wt.) and pressed and sieved to retain aggregates 0.125–0.18 mm in diameter. These aggregates were loosely mixed with non-porous quartz granules of similar size (acid-washed, Fluka) in order to avoid any intraparticle or bed gradients in concentration or temperature, which would corrupt the intended kinetic origins of measured rates. These samples were placed as packed beds within stainless steel tubes in reactor configurations that ensured plug-flow hydrodynamics.

Samples were treated in flowing H_2 (Praxair, 99.999 %) at 673 K (Ru and Pt) and 773 K (Re) or in flowing 5 % H_2S/He (Praxair, certified mixture) at 773 K (ReS_x) for 1 h before kinetic measurements. These treated samples were cooled to reaction temperatures (623 K for Ru, 573 K for Pt and Re), and H_2 (Praxair, 99.999 %) and H_2S/H_2 (Praxair, certified mixtures) were introduced using electronic flow controllers (Parker, Series 201). The reactor pressure was set using a dome-loaded pressure regulator (Mity Mite). Thiophene (Alfa Aesar, 99 %) was introduced as a mixture with n-decane (Aldrich, 99+%, internal standard; 50 kPa) using a high-pressure pump (Isco 500D) and vaporized upon introduction into lines kept above 433 K in order to prevent condensation. Inlet and outlet streams were analyzed by gas chromatography (Agilent 6890) using a methyl silicone capillary column (HP-1, Agilent, 25 m ×0.32 mm ×0.52 μm) connected to a flame ionization detector and a Porapak Q packed column (Supelco, 1.82 m ×3.18 mm, 80–100 mesh) connected to a thermal conductivity detector.

Rates and selectivities were measured over a range of H_2 (1−3 MPa), thiophene (1−10 kPa), and H_2S (0.2−10 kPa) pressures at thiophene conversions below 15 % in order to maintain differential conditions; the bed residence time was varied in order to determine the relative contributions of primary and secondary reactions. Rates are reported as turnover rates normalized by the number of exposed metal atoms determined from dispersion values derived from chemisorption uptakes (Section 2.2) for Ru, Pt, and Re and by the total number of Re atoms for the highly dispersed lamellar structures observed in ReS_x.

Table 1
Treatments used for the synthesis of SiO_2-supported Ru, Pt, Re, and ReS_x nanostructures.

Catalyst (nominal weight loading/mean particle size[a])	Dry air treatment[b] temperature (K)/time (h)/ramp (K s^{-1})	H_2 treatment[c] temperature (K)/time (h)/ramp (K s^{-1})
Ru (1 %/1.6 nm)	–	723 / 2 / 0.083 [d]
Pt (0.3 %/4.8 nm)	823 / 5 / 0.05	673 / 1 / 0.033 [d]
Re (15 %/6.9 nm)	573 / 3 / 0.033	773 / 2 / 0.05 [e]
ReS_x (15 %/n/a[f])	573 / 3 / 0.033	– [g]

[a] Determined by H_2 or O_2 chemisorption uptakes [8,9,15]; H:Pt_s = 1:1, H:Ru_s = 1:1, O:Re_s = 0.4:1.
[b] 99.99 % extra dry air, Praxair, 1.0 $cm^3\ g^{-1}\ s^{-1}$; treatment before subsequent H_2 treatments.
[c] Treatment (passivation), employed after H_2 treatment, in 0.1–0.5 % O_2/He (Praxair, certified mixture); 0.05–1.0 $cm^3\ g^{-1}\ s^{-1}$ at ambient temperature for 2–6 h.
[d] 9 % H_2/He, Praxair (HY-9C), 1.67 $cm^3\ g^{-1}\ s^{-1}$.
[e] 99.999 % H_2, Praxair (HY-5.0UH), 1.0 $cm^3\ g^{-1}\ s^{-1}$.
[f] Anisotropic, layered nanostructures.
[g] Subsequent treatment in 5 % H_2S/He, Praxair (certified mixture), 45 $cm^3\ g^{-1}\ s^{-1}$, 2 h, 0.05 K s^{-1}.

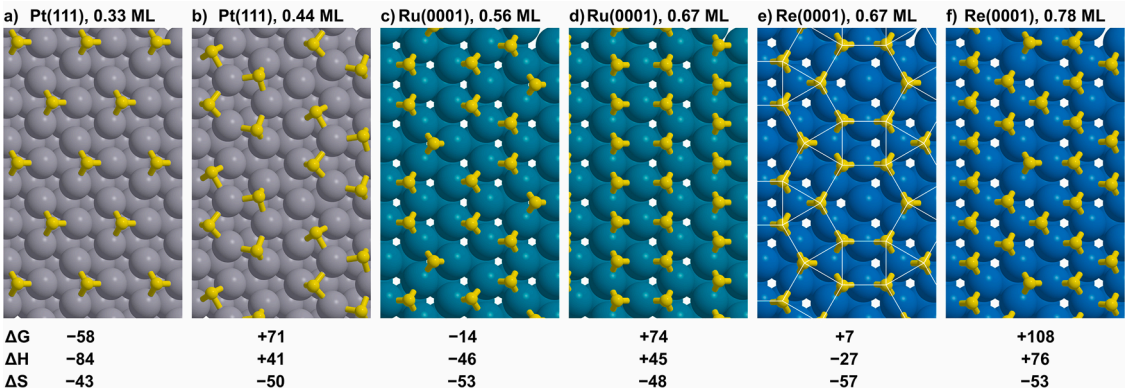

Fig. 1. Coverages of S adlayers on close-packed Pt, Ru, and Re surfaces at 1/3–7/9 ML coverage. Differential S adatom formation from H_2S decomposition and H_2 evolution (Eq. (4)) free energies, enthalpies, and entropies are shown below each structure.

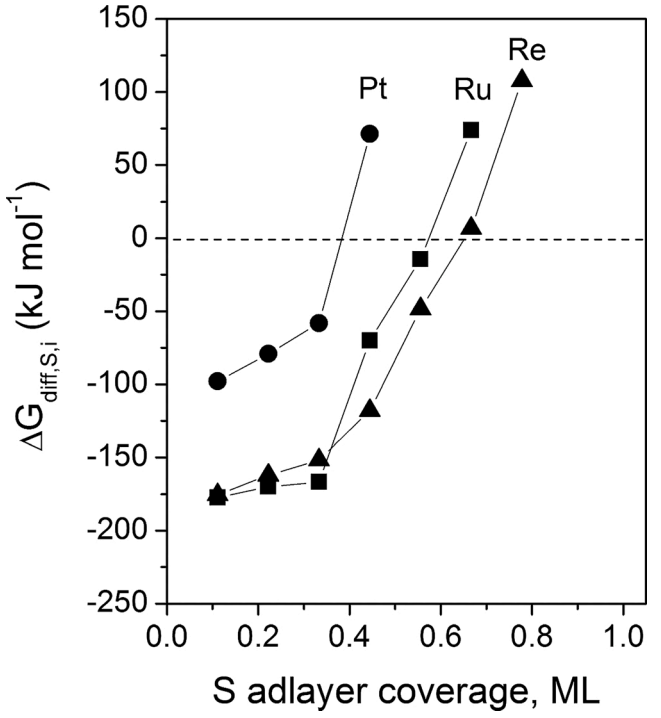

Fig. 2. S adatom formation free energy ($\Delta G_{diff,S,i}$) to form S* and gaseous H_2 (Eq. (4)), determined by DFT on 3 × 3 unit cells of close packed surfaces of Pt (111) (●), Ru(0001) (■), and Re(0001) (▲), as a function of S adlayer coverage. Enthalpies and entropies corresponding to these data are shown in Table S.1-3 (SI, S.1).

2.4. Density functional theory methods for examining S adsorption

Periodic plane-wave DFT calculations were carried out using the Vienna ab initio simulation package (VASP) [23–26] as implemented in the computational catalysis interface (CCI) [27]. Plane waves were constructed using projector-augmented wave (PAW) potentials with an energy cutoff of 400 eV [28,29]. The revised Perdew-Burke-Ernzerhof (RPBE) form of the generalized gradient approximation (GGA) was used to describe exchange-correlation energies [30–32]. Structural optimization calculations were performed in two steps, with each step optimizing the structure until the force on any atom was < 0.05 eV $Å^{-1}$. In the first step, wavefunctions were converged to within 10^{-4} eV and forces were calculated using a fast Fourier transform (FFT) grid of 1.5× the plane-wave cutoff. In the second step, wavefunctions were converged to within 10^{-6} eV and forces were calculated using a FFT grid two times the plane-wave cutoff, as these settings provide more accurate forces. Both geometric convergence calculations were performed using a 4 × 4 × 1 sampling of the Brillouin zone. A single-point calculation energy calculation at an 8 × 8 × 1 sampling was used to compute the final electronic energies.

Sulfur adsorption energies were modeled on 3 × 3 slabs of Ru(0001) (a =2.7059 Å, b =4.2815 Å), Re(0001) (a =2.761 Å, b =4.456 Å), and Pt (111) (a =3.9239 Å) with four metal layers and a 10 Å vacuum region. The bottom two metal layers of these slabs were fixed at their bulk crystallographic positions, while all other atoms were allowed to relax during structural optimization calculations. Adsorption energies were also calculated on cubo-octahedral 201-atom Ru, Re, and Pt fcc clusters [33–38] in order to confirm that periodic surface models did not introduce lateral relaxation artifacts.

Frequency calculations were carried out using a fixed displacement method with two displacements per degree of freedom for many structures, as described in more detail below. For surface calculations, all metal atoms were fixed and all S* atoms were displaced to calculate their vibrational frequencies. For gas-phase calculations, all atoms were displaced. Wavefunctions were converged to within 10^{-6} eV and forces calculated using a FFT grid two times the plane-wave cutoff. Frequency calculations were not performed for the nanoparticle models. These frequency calculations were used to determine zero-point vibrational energies (ZPVE) and temperature-corrected enthalpies (*H*) and free energies (*G*) using the harmonic oscillator approximation to estimate vibrational partition functions, and these methods were combined with

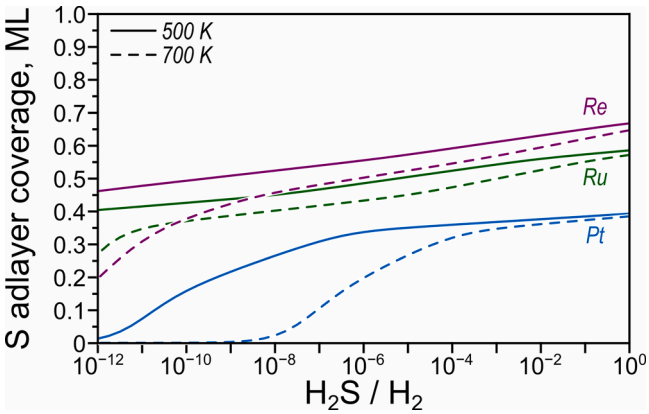

Fig. 3. S adlayer coverage with varying H_2S/H_2 on Pt(111) (blue), Ru(0001) (green), and Re(0001) (purple) at 500 K (solid line) and 700 K (dashed line).

rotational and translational partition functions for ideal gas molecules to calculate their enthalpies

$$H = E_0 + ZPVE + H_{vib} + H_{trans} + H_{rot} \quad (2)$$

and free energies

$$G = E_0 + ZPVE + G_{vib} + G_{trans} + G_{rot} \quad (3)$$

at 500–700 K.

Sulfur atom adlayers on Ru(0001), Re(0001), and Pt(111) close-packed surfaces were examined at coverages between 1/9–1 ML (monolayer) on 3 × 3 surface unit cells (1–9 S-atoms per cell). At each coverage, several symmetrically distinct arrangements of S adatoms initially bound in atop, three-fold fcc, and three-fold hcp sites (and mixtures) were examined. At each coverage, the minimum-E_0 S adatom configuration was further examined with vibrational frequency calculations to calculate enthalpies, entropies, and free energies. During desulfurization reactions, coverages of chemisorbed S (S*) are set by the prevalent H_2S/H_2 ratios through

$$H_2S(g) + * \leftrightarrow S^* + H_2(g) \quad (4)$$

when such a reaction is equilibrated:

$$\Delta G^0 = -RT\cdot\ln(K_{S,ad}) = -RT\cdot\ln\left(\frac{P_{H_2S}}{P_{H_2}}\right) \quad (5)$$

where ΔG° is the Gibbs free energy for the formation of bound S-atoms via Eq. (4), $K_{S,ad}$ is the equilibrium constant for such formation, and P_{H2S} and P_{H2} are the gas phase pressures of H_2S and H_2. Sulfur atom adlayers on 201-atom Ru, Re, and Pt particles were generated by placing S-atoms at all three-fold hcp sites on (111) terraces, all bridge sites on edges between (111) terraces, and four-fold hollow sites on (100) terraces. These adlayers contained 96–144 S atoms (0.79–1.18 ML, defined as S: M_{surf} ratio); for each adlayer, a single S* was removed from the (111) terrace to determine differential adsorption energies.

DFT-derived Gibbs free energies were calculated at each coverage on Ru(0001), Re(0001), and Pt(111) models and denoted as S adatom formation energies. Differential formation energies were calculated between minimum-energy S adlayer configurations from 1/9 to 1 ML (as defined by the coverage of the product state in Eq. (4)) as

$$\Delta E_{diff,S,i} = E[S^*_i] + E[H_2(g)] - E[S^*_{i-1}] - E[H_2S(g)] \quad (6)$$

based on the energy of the gas-phase species (H_2 and H_2S) and surface S adlayer ensembles with i and $i-1$ S adatoms. S adatom formation free energy ($\Delta G_{diff,S,i}$) can be used to obtain a temperature-dependent equilibrium constant that is a function of S adlayer coverage:

$$K_{S,ad}(T,\theta_S) = \exp\left(-\frac{\Delta G_{diff,S,i}}{RT}\right) \quad (7)$$

which can be used to estimate coverage as a function of the H_2S/H_2 ratio.

3. Results and discussion

3.1. Nature of S adlayers on Pt, Ru, and Re metal surfaces

Ru and Pt persist as bulk metal clusters at the temperatures and

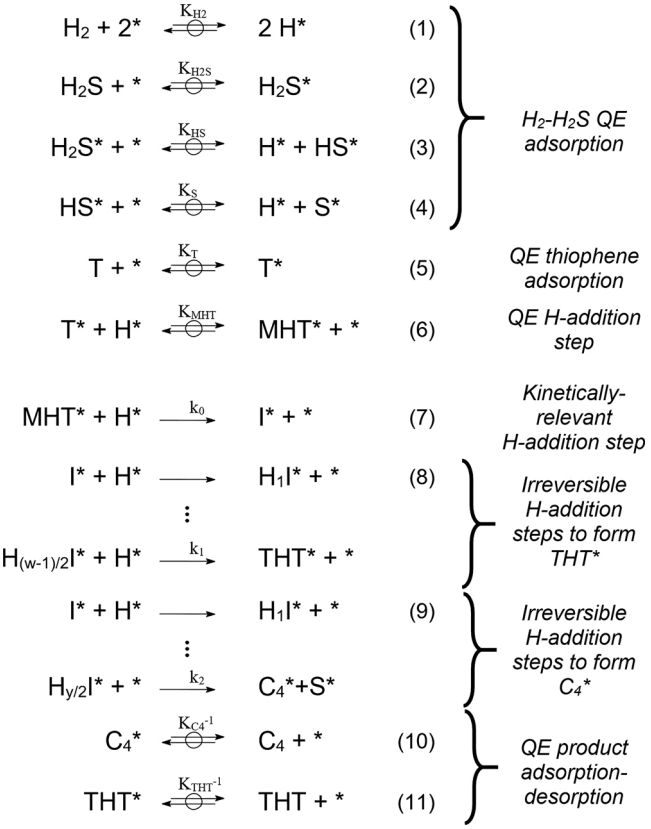

Scheme 1. Elementary steps for thiophene conversion and desulfurization-hydrogenation pathways on Ru and Pt. Reactant and product desorption occur on *, the interstices within refractory surface templates of S adatoms, on Ru and Pt. Adsorbed species are bound on * and include hydrogen (H*), hydrogen sulfide (H_2S^*), sulfhydryl (HS*), sulfur (S*), thiophene (T*), and monohydrothiophene (MHT*), which form via quasi-equilibrated adsorption/desorption steps. Thiophene consumption is mediated by the addition of H* to MHT* (Step 7), which forms an intermediate (I*) common to both the formation of tetrahydrothiophene (THT) and butene/butane (C_4) products, via subsequent surface reactions (Steps 8 and 9) and desorption (Steps 10 and 11).

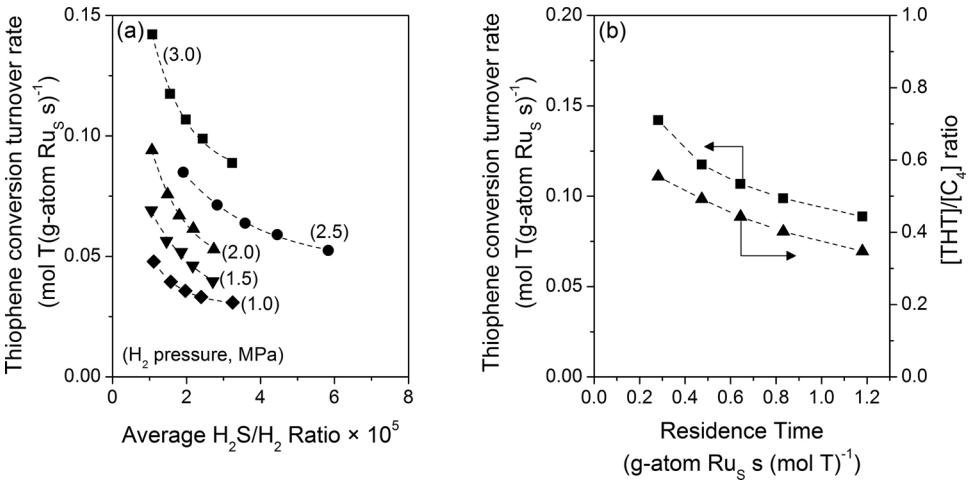

Fig. 4. (a) Turnover rates for thiophene conversion measured without added H_2S as a function of average H_2S/H_2 ratio, at 623 K, 2.5 kPa thiophene and 1.0 MPa (◆), 1.5 MPa (▼), 2.0 MPa (▲), 2.5 MPa (●), or 3.0 MPa (■) H_2 on Ru/SiO_2 and (b) turnover rates (■) and tetrahydrothiophene (THT) to butene/butane (C_4) concentration ratios (▲) measured without added H_2S as a function of residence time at 623 K, 2.5 kPa thiophene, and 3.0 MPa H_2 on Ru/SiO_2. Average H_2S/H_2 ratios are based on the average of inlet and effluent H_2S concentrations measured at each residence time.

sulfur chemical potentials in this study (573–623 K, 10^{-4}–10^{-2} H_2S/H_2). Their surfaces, however, become decorated by strongly bound S-atoms derived from S-containing reactants or added H_2S [8,9] at all conditions; as a consequence, reactions such as alkane hydrogenolysis and dehydrogenation are strongly and irreversibly inhibited by S adatoms, even after S-containing molecules (e.g., H_2S) are removed from reactants. DFT-derived free energies of S adatom formation from H_2S (forming H_2, $\Delta G_{diff,S,i}$, Eq. (4), 600 K and 1 bar) are more negative than −150 kJ mol^{-1} at coverages up to 1/3 ML on Ru(0001) and Re(0001) and more negative than −50 kJ mol^{-1} at coverages up to 1/3 ML on Pt (111). Within this coverage range, S binds to Re(0001), Ru(0001), and Pt(111) surfaces on three-fold sites fcc (Pt) or hcp (Ru and Re) sites, which differ only in the presence of another atom directly beneath these hollow sites in either the third (fcc) or second (hcp) atom layer. Sulfur adatoms arrange to maximize their S–S distances, as determined by comparing multiple arrangements at 2/9 (Table S.1-2; SI, S.1) and 1/3 (Fig. S.1-1; SI, S.1) ML coverage, with the latter reflecting the maximum coverage of three-fold bound adatoms that allows binding without sharing surface atoms (Fig. 1a for Pt). $\Delta G_{diff,S,i}$ values sharply increase from −167 kJ mol^{-1} at 1/3 ML to −70 kJ mol^{-1} at 4/9 ML on Ru(0001) and increase from −58 to +71 kJ mol^{-1} on Pt(111) (over the same range of coverages, Fig. 2) as S adatoms are forced to share metal atoms at 4/9 ML and higher coverages.

On Pt(111), DFT-derived free energies show that sulfur coverages are not likely to exceed 1/3 ML at H_2S/H_2 ratios prevalent during HDS catalysis (10^{-5}–10^{-2}). The large and positive $\Delta G_{diff,S,i}$ of +71 kJ mol^{-1} (600 K, 1 bar) at 4/9 ML on Pt(111) (Fig. 2) indicates that they would not be stable even at H_2S/H_2 ratios near unity. At 4/9 ML, Pt(111) surfaces (Fig. 1b) form sulfur adlayers that maximize S–S distances by binding at a combination of three-fold fcc and hcp sites; such coverages lead to significant surface distortion, with metal atoms protruding from the surface, as also observed upon formation of dense oxygen adlayers on noble metals [39]. Above 4/9 ML, bound S_2* dimers form spontaneously during adlayer optimization because weak M—S bonds (at these coverages) allow their cleavage to be compensated by the formation of S—S bonds; consequently, $\Delta G_{diff,S,i}$ values are reported up to 4/9 ML coverages, the highest coverage before S_2* formation.

Ru(0001) and Re(0001) surfaces, in contrast, achieve higher sulfur coverages than Pt(111), without detectable formation of S_2* or surface restructuring (up to 1 ML). On Ru and Re surfaces, $\Delta G_{diff,S,i}$ increase, indicating less stable adsorption, at coverages above 1/3 ML (with Ru showing an abrupt increase at 1/3 ML; Fig. 2). On Ru(0001), $\Delta G_{diff,S,i}$ values increased from −14 kJ mol^{-1} at 5/9 ML (Fig. 1c) to +74 kJ mol^{-1} at 2/3 ML (Fig. 1d), indicating that working surfaces are not likely to reach 2/3 ML for Ru(0001) surfaces. S adlayers at 5/9 ML form a pentagonal pattern with S-atoms located at a combination of three-fold fcc and hcp sites. At 6/9 ML, the adlayer adopts a striped pattern, which was found to be the most stable arrangement among ~30 distinct S* configurations. On Re(0001), $\Delta G_{diff,S,i}$ values increase monotonically with increasing sulfur coverage and $\Delta G_{diff,S,i}$ values are +7 kJ mol^{-1} at 2/3 ML, suggesting that surfaces would reach 2/3 ML at H_2S/H_2 ratios near unity at 600 K. The sulfur adlayer at 2/3 ML coverages (Fig. 1e) forms a rhombitrihexagonal tiling (3.4.6.4 tessellation) with half of the atoms in three-fold fcc sites and half in three-fold hcp sites. The $\Delta G_{diff,S,i}$ involved in forming the 7/9 ML sulfur coverages (Fig. 1f) is +108 kJ mol^{-1}, with S-atoms occupying three-fold hcp and fcc sites in a 6:1 ratio. S–S adatom repulsion causes $\Delta G_{diff,S,i}$ values to increase by about 400 kJ mol^{-1} from 1/9 ML to 1 ML on Ru(0001) and by about 300 kJ mol^{-1} on Re(0001), as a consequence of coulombic S*–S* repulsion at these coverages.

These DFT-derived free energies show that sulfur adlayers, even at high H_2S/H_2 ratios, retain interstices on Pt, Ru, and Re surfaces that may reversibly interact with bound intermediates and transition states involved in thiophene conversion reactions. Previous studies have indicated that periodic surface models, such as those used here, can lead to the inaccurate prediction of saturation at sub-monolayer coverages for CO* (on Ru) and NO* (on Rh) [33–35,38]. The conclusion that sulfur adlayers retain bare interstices at H_2S/H_2 ratios prevalent during HDS catalysis was confirmed here from calculations on cubo-octahedral fcc 201-atom cluster models of Ru, Re, and Pt, as discussed in detail in the Supporting Information (Section S.2). Indeed, bare interstices persist on those particles, as shown by differential adsorption energies that were positive at 1 ML coverages. The large and negative $\Delta G_{diff,S,i}$ values (−176 to −58 kJ mol^{-1}) for S* formation at low coverages (1/9 to 1/3 ML) on Pt(111), Ru(0001), and Re(0001) surfaces indicate that such bound S-atoms act as irreversible titrants during catalysis.

DFT-derived $\Delta G_{diff,S,i}$ values can be used to estimate S* coverages at each temperature and H_2S/H_2 ratio and adsorption equilibrium constants ($K_{S,ad}$) at each coverage (Fig. 3). DFT-predicted sulfur coverages on Pt(111) are essentially constant (0.35–0.36 ML) at the conditions employed in this study (573 K, 10^{-4}–10^{-3} H_2S/H_2), as are those on Ru (0001) (0.51–0.55 ML, 623 K, 10^{-4}–10^{-2} H_2S/H_2) and Re(0001) (0.55–0.60 ML, 573 K, 10^{-5}–10^{-3} H_2S/H_2). These coverages, furthermore, do not significantly decrease even at H_2S/H_2 ratios as low as 10^{-12} on Ru and Re and 10^{-6} on Pt. These data suggest that, on a given metal surface, a fixed fraction of these S adatoms (S′) remain on the surface and compose a refractory S′ adlayer that cannot be removed even in the effective absence of H_2S. This fraction ($\theta_{S'}$), however, depends on the metal, with Re ($\theta_{S'}$ ~5/9 ML) > Ru ($\theta_{S'}$ ~1/2 ML) > Pt ($\theta_{S'}$ ~1/3 ML), reflecting the density of the S′ adlayer that forms. These fractional

coverages of S′, predicted from DFT, seem consistent with experimental S adsorption on single crystal surfaces, which reach saturated ordered structures (0.4–0.6 ML) on close-packed surfaces (e.g., c(7×√3)rect.-3S on Pt(111) surfaces [40]; (√3×√3)R30° on Re(0001) [41]). The remaining, uncovered fraction of the surface (i.e., $1-\theta_{S'}$) must therefore bind S more weakly, as shown by the large and positive H_2S formation energies on Re (>5/9 ML), Ru (>1/2 ML), and Pt (>1/3 ML); these interstitial sites form a passivated surface on which reactants and intermediates bind. Indeed, S-binding energies reportedly decrease sharply as these S′ adlayers are formed on metal nanoparticle surfaces [42–46] but reach a constant value before reaching surface saturation, thus leaving passivated spaces that can bind S-atoms weakly and reversibly, as S* species whose surface concentration can vary with sulfur chemical potential.

Thiophene reactions take place on the interstices (*) within these unreactive adlayers consisting of stable ordered S′-structures. The interstitial metal vacancies (*) within these S′-passivated surfaces bind transition states and adsorbates reversibly. This "partitioning" of surfaces into an unreactive S′ adlayer and reactive interstitial metal sites (*) that can reversibly-bind adsorbates (as necessary for catalytic turnover) permits Langmuirian kinetic treatments to be applied to the interstitial regions. Turnover rates per total number of exposed metal atoms (absent S) therefore depend on the fraction of the surface occupied by the refractory S′ adlayer and the reactivity of the remaining interstitial spaces.

3.2. Thiophene conversion turnover rates on Ru and Pt

Thiophene molecules react to form saturated cyclic products (tetrahydrothiophene (THT) and dihydrothiophene (DHT)), acyclic hydrocarbons (butadiene, 1-butene, cis-2-butene, trans-2-butene, and butane), and H_2S through reactions on active interstices within unreactive S′ adlayers. Butene regioisomers are equilibrated and treated here as lumped chemical species ($C_4^=$). H_2 and H_2S dissociation on accessible sites (*) (Steps 1.1–1.4; Scheme 1) are equilibrated steps, as evidenced by isotopic scrambling experiments [8,9], such that they can be described by a combined reaction (Eq. (4)) and to S* coverages set by H_2S/H_2 ratios Eqs. (5) and (7).

Such equilibria lead to sulfur coverages and chemical potentials set by prevalent H_2S/H_2 ratios, which lead, in turn, to axial gradients in S*, bound on the surfaces that are accessible during catalysis, as thiophene converts, unless H_2S is present at the bed inlet. Such gradients and their kinetic consequences are evident from measured rates with H_2-thiophene reactant mixtures (without added H_2S) that decrease with increasing bed residence even at low thiophene conversions (e.g., 0.14 to 0.09 mol thiophene (g-atom Ru_s s)$^{-1}$ as residence times increase 0.28 to 1.2 s g-atom Ru_s (mol thiophene)$^{-1}$; 4–10 % conversion; Fig. 4b). These trends reflect the strong inhibition caused by the equilibrium of the reaction shown as Eq. (4) as S* replaces * at surfaces. The sharp gradients in sulfur chemical potential near the bed inlet cannot be captured accurately through changes in bed residence time in the absence of co-fed H_2S; differential reactor behavior requires the presence of H_2S at inlet concentrations higher than those formed from thiophene. The combined contributions of H_2S concentration and secondary reactions to a relative abundance of products with changes in bed residence time cannot be accurately dissected except through such experimental protocols.

At any given bed residence time, rates measured without inlet H_2S reflect the axial average of such rates along a bed with strong axial gradients in S* coverages. This leads to inaccurate extrapolations to the bed inlet conditions because of the strong effects of H_2S/H_2 ratios on rates and selectivities (e.g., Fig. 4b). Such (extrapolated) rates (Fig. 5, open squares) reflect the combined effects of conversion on axial H_2S/H_2 ratios and the extent of secondary reactions of THT. These inextricable phenomena lead to an apparent sublinear increase in extrapolated rates as H_2 pressures increase (Fig. 5, open squares), which can be misconstrued as a consequence of abundant H_2-derived bound species [8]; they also lead to a decrease in THT/C_4 product ratios with increasing residence time (Fig. 4b).

These selectivity trends reflect the greater extent of fast secondary THT reactions as conversion increases with increasing residence time. The higher THT/C_4 product ratios observed at low thiophene conversions, which are more prevalent at higher inlet H_2S/H_2 ratios, may give the impression that THT formation is facilitated by H_2S, via a kinetic route distinct from that for C_4 formation [8,9]. Such conclusions, however, do not consider the role of secondary THT reactions on measured selectivities, which depend strongly on thiophene conversion.

Thiophene conversion rates on Ru/SiO_2 decreased as the average H_2S/H_2 ratios increased along the bed with increasing thiophene conversion, at all H_2 pressures (1−3 MPa; Fig. 4a); this is consistent with the strong inhibition effects caused by bound H_2S-derived species. Such average H_2S/H_2 ratios become rigorous descriptors of their kinetic consequences only when rates are proportional to such ratios. In fact, strong inhibition effects lead to a singularity at the bed inlet and to very high rates near the bed inlet. These data, however, can be interpolated to assess H_2 pressure effects at a given H_2S/H_2 to give, in turn, the strictly first-order dependence of rates on H_2 pressure shown in Fig. 5. This is also evident from H_2 pressure effects measured with added H_2S (inlet H_2S/H_2 ratios $\geq 3.0 \times 10^{-3}$) so as to maintain constant sulfur chemical potentials along the bed (Fig. 6). Such linear dependences show that the sublinear effects of H_2 pressure on rates reported previously [8] reflect imperfect extrapolations of rates and selectivities to the conditions at the bed inlet instead of the presence of any kinetically-detectable H_2-derived bound intermediates on the active Ru surfaces.

3.3. Identity and kinetic relevance of bound intermediates and elementary steps on Ru and Pt nanoparticles

Thiophene conversion turnover rates on Ru and Pt decreased with increasing inlet H_2S/H_2 ratios (Figs. 7 and 8), indicating that S* competes with any chemisorbed H* or thiophene-derived intermediates for the interstitial sites (*) on working surfaces. These labile S* species (and not the permanent unreactive S′ atoms that form the refractory layer) respond via equilibration with the contacting H_2S/H_2 ratio (Eq. (4)), as shown by fast isotopic H_2/D_2 and H_2S/D_2S scrambling during thiophene reactions [8,9] and from rates that respond reversibly to changes in H_2S/H_2 ratios. The effects of H_2S/H_2 on rates reflect the inhibition as reversibly bound S* species occupy the reactive interstitial sites (*) and not of any change in the fraction ($\theta_{S'}$) of exposed surfaces covered by the permanent S′ adlayer (Section 3.1).

Rates increased with increasing H_2 (Figs. 6 and 9) and thiophene (Figs. 7 and 8, triangles) pressures, consistent with kinetically-relevant transition states that contain thiophene-derived species and H-atoms derived from H_2. The sublinear rate increase with thiophene pressure reflects the consequences of detectable coverages of active interstices by thiophene-derived species leading to a term in the denominator of a Langmuirian-type rate equation.

These kinetic trends on Ru and Pt are described accurately by rate equations that contain a first-order dependence on H_2 and thiophene pressures in the numerator [8,9], but with denominator terms that account for the relative coverages on active sites, the number of which ([L]) depends on the fraction of the total surface occupied by the refractory S′ adlayer. These active surfaces for both thiophene conversion routes exist as interstices within a refractory S′ adlayer and with labile sulfur (S*) coverages set by equilibrated H_2-H_2S interconversions (Steps 2.10–2.13; Scheme 2), as described in Scheme 1. Thiophene conversion rates are then described by the rate equation:

$$\frac{r}{[L]} = \frac{\alpha(H_2)(T)}{\left(1 + \beta(H_2)^{0.5} + \gamma(T) + \eta\,(H_2S)/(H_2)\right)^2} \quad (8)$$

where the denominator terms of Eq. (8) represent the relative coverages of vacant interstitial sites (*) (Eq. 2.15; Scheme 2). This equation

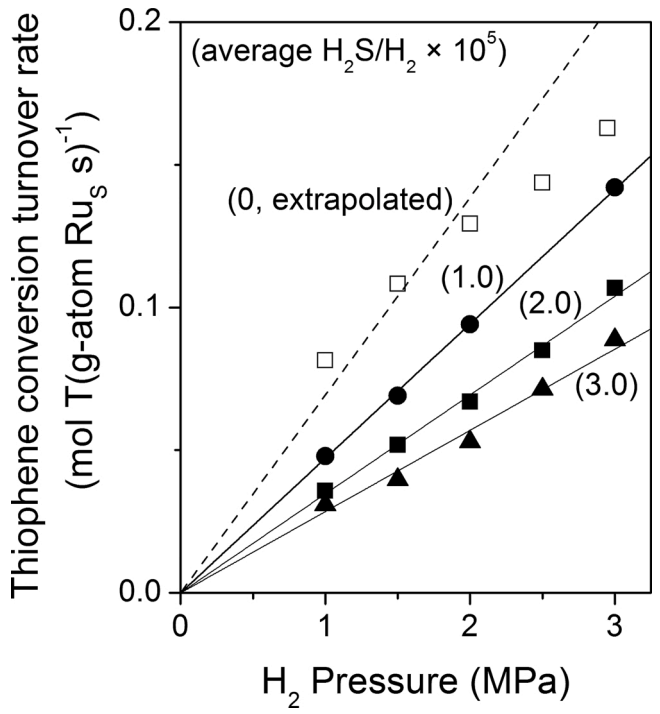

Fig. 5. Turnover rates for thiophene conversion as a function of H_2 pressure, at 623 K, 2.5 kPa thiophene, obtained from interpolating data (Fig. 4) at average H_2S/H_2 ratios of 3.0×10^{-5} (▲), 2.0×10^{-5} (■), or 1.0×10^{-5} (●). Lines indicate first-order dependences on H_2 pressure. For comparison, rates (from [8]) derived from linear extrapolation of measured rates to zero residence time, without added H_2S, are also plotted (□).

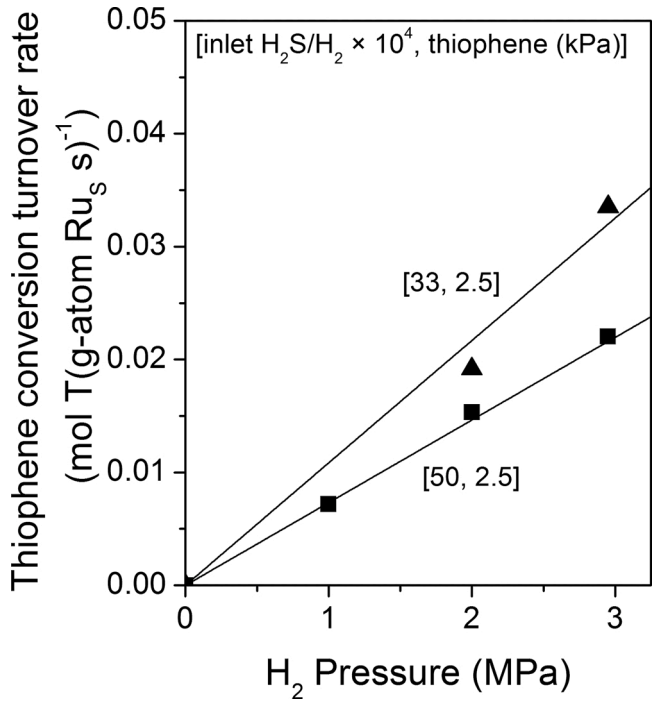

Fig. 6. Turnover rates for thiophene conversion at 623 K as a function of H_2 pressure (at 2.5 kPa thiophene, and 3.3×10^{-3} (▲) or 5.0×10^{-3} (■) inlet H_2S/H_2 ratios) on Ru/SiO_2. Curves reflect regression of all measured rate data (on Ru) to the functional form of Eq. (11).

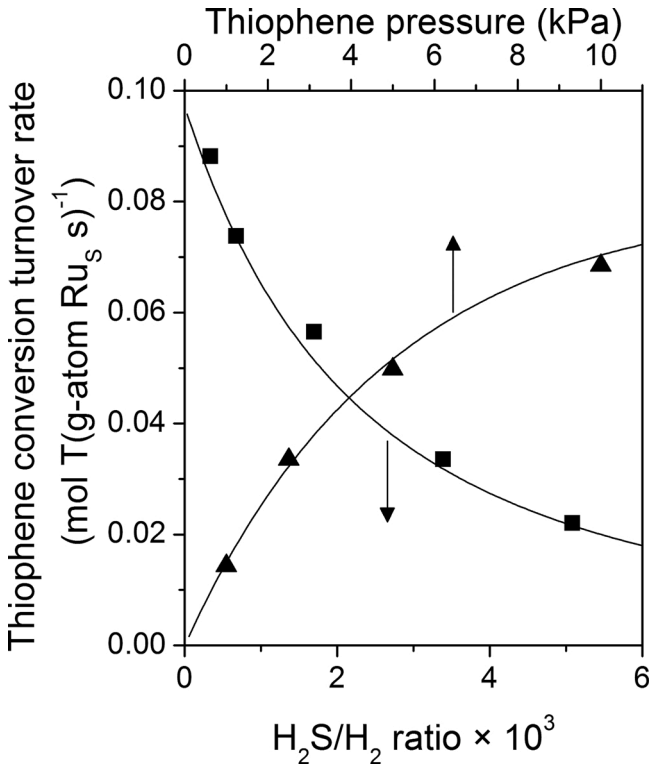

Fig. 7. Turnover rates for thiophene conversion at 623 K as a function of thiophene pressure (at 3.0 MPa H_2 and 3.3×10^{-3} inlet H_2S/H_2 ratio (▲)) and of inlet H_2S/H_2 ratio (at 2.5 kPa thiophene and 3.0 MPa H_2 (■)) on Ru/SiO_2. Curves represent regression of all measured data (on Ru) to the functional form of Eq. (11).

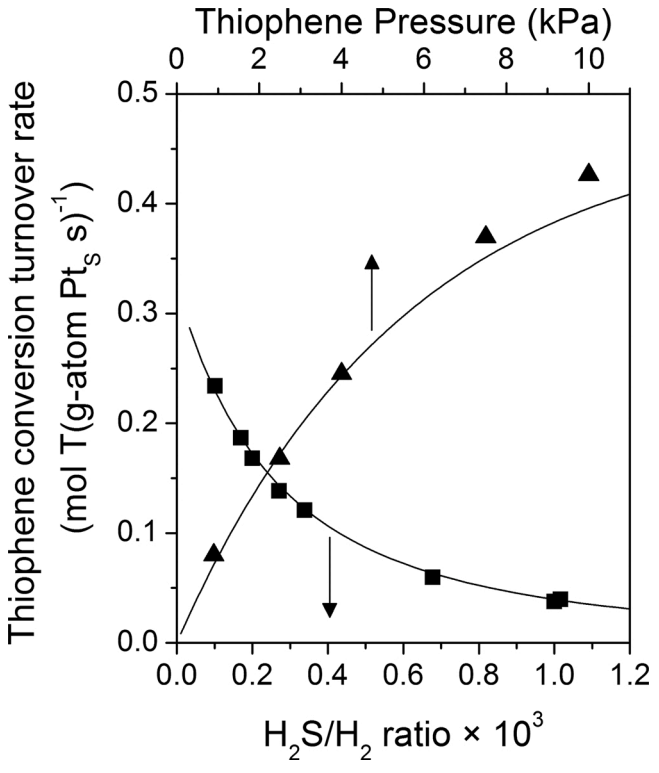

Fig. 8. Turnover rates for thiophene conversion at 573 K as a function of thiophene pressure (at 3.0 MPa H_2 and 2.0×10^{-4} inlet H_2S/H_2 ratio (▲)) and of inlet H_2S/H_2 ratio (at 2.5 kPa thiophene and 3.0 MPa H_2 (■)) on Pt/SiO_2. Curves represent regression of all measured data (on Pt) to the functional form of Eq. (12).

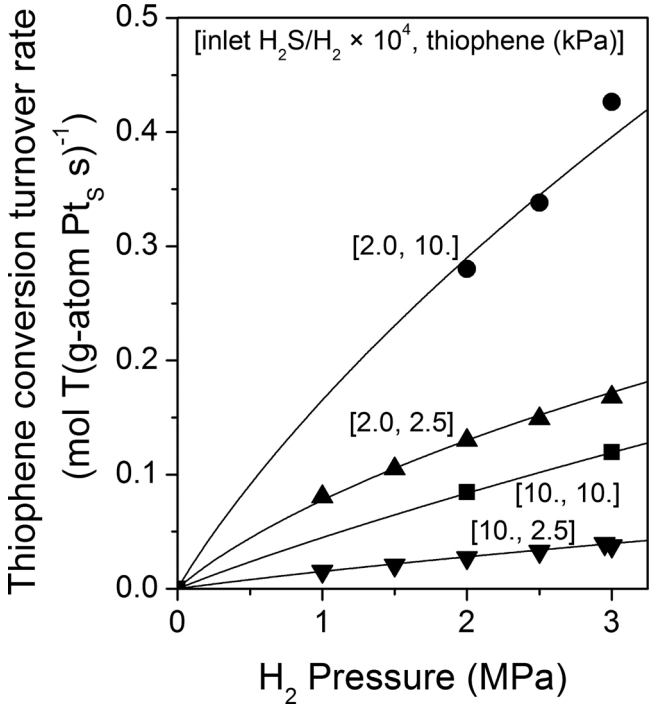

Fig. 9. Turnover rates for thiophene conversion at 573 K as a function of H_2 pressure at 2.5 kPa thiophene (2.0×10^{-4} (▲) or 1.0×10^{-3} (▼) inlet H_2S/H_2 ratio) and at 10 kPa thiophene (2.0×10^{-4} (●) or 1.0×10^{-3} (■) inlet H_2S/H_2 ratio) on Pt/SiO_2. Curves reflect regression of all measured data (on Pt) to the functional form of Eq. (12).

corresponds to the elementary steps in Scheme 1 with quasi-equilibrated reactant adsorption and pseudo-steady state coverages for all bound species (e.g., bound thiophene (T*), bound monohydrothiophene (MHT*)). These assumptions lead, in turn, to a numerator term consistent with the addition of H* to MHT* as the kinetically-relevant step (Step 1.7; Scheme 1). The lumped coefficients in Eq. (8) are described in terms of the kinetic and thermodynamic parameters for these elementary steps (Scheme 1), whose values are listed in Table 2. Turnover rates are reported based on the number of atoms exposed at nanoparticle surfaces (as measured by chemisorption uptake experiments; Section 2.2), but only some ([L]; Eq. (8)) remain accessible within the refractory S′ adlayers prevalent during catalysis. Reported turnovers thus relate to the Langmuirian rate expression (Eq. (8)) by a factor $(1-\theta_{S'})$, which represents the fraction of the exposed surfaces not covered by the refractory (unreactive) S′ adlayer:

$$\frac{r}{[L]+[S']} = \frac{r}{[L]}\left(\frac{[L]}{[L]+[S']}\right) = \frac{r}{[L]}(1-\theta_{S'}) \quad (9)$$

The concentration of these S adatoms ([S′]) remains constant as H_2S/H_2 ratios vary over the relevant range (Section 3.1), and thus, the functional form of the rate equation and the chemical significance of its regressed parameters are unaffected by any site-count normalizations except for the interpretation of the lumped rate constant in the numerator (α; Eq. (8)):

$$\alpha_{measured} = \alpha(1-\theta_{S'}) \quad (10)$$

Previous formalisms [8,9] invoked heterolytic H_2 and H_2S dissociation steps and thiophene adsorption on vacancy-sulfur (#—S′) site pairs, as well as the premise that surfaces were nearly-covered with S adatoms during HDS catalysis (Steps 2.1–2.4; Scheme 2). These interpretations implicated the formation (via H_2 and H_2S dissociation on these site pairs) and involvement of charged H-species ($H^{\delta+}$, $H^{\delta-}$) in thiophene desulfurization and hydrogenation, as invoked by others in the literature [16,17,47,48]. The increase in THT/C_4 ratios with increasing H_2S

	Dissociation and adsorption on sulfur-vacancy site pairs[1]		H_2-H_2S dissociation on * within refractory S′ adlayer	
Quasi-equilibrated adsorption / dissociation steps	(1) $H_2(g) + \#-S' \rightleftarrows \#H^{\delta-}-S'H^{\delta+}$	K_{H2}	(10) $H_2(g) + 2* \rightleftarrows 2H*$	K_{H2}
	(2) $H_2S(g) + \#-S' \rightleftarrows \#SH^{\delta+}-S'H^{\delta+}$	K_{H2S}	(11) $H_2S(g) + * \rightleftarrows H_2S*$	K_{H2S}
	(3) $\#SH^{\delta+}-S'H^{\delta+} + \#-S' \rightleftarrows \#H^{\delta-}-S'H^{\delta+} + \#S-S'$	K_S	(12) $H_2S* + * \rightleftarrows HS* + H*$	K_{HS}
			(13) $HS* + * \rightleftarrows S* + H*$	K_S
	(4) $T(g) + \#-S' \rightleftarrows \#T-S'$	K_T	(14) $T(g) + * \rightleftarrows T*$	K_T
Langmuir Site Balance	$[L] = (\#-S') + (\#H^{\delta-}-S'H^{\delta+}) + (\#T-S') + (\#SH^{\delta+}-S'H^{\delta+}) + (\#S-S')$		$[L] = (*) + (H*) + (T*) + (S*)$	
	(5) $[L] = (\#-S')\cdot\left[1+\beta(H_2)+\gamma(T)+\delta(H_2S)+\eta\frac{(H_2S)}{(H_2)}\right]$		(15) $[L] = (*)\cdot\left[1+\beta(H_2)^{0.5}+\gamma(T)+\eta\frac{(H_2S)}{(H_2)}\right]$	
β	(6)	K_{H2}	(16)	$K_{H2}^{0.5}$
γ	(7)	K_T	(17)	K_T
δ	(8)	K_{H2S}		--
η	(9)	$K_S K_{H2S} K_{H2}^{-1}$	(18)	$K_S K_{HS} K_{H2S} K_{H2}^{-1}$

[1] adapted from [8,9]

Scheme 2. Equilibrated H_2-H_2S dissociation on sulfur-vacancy pairs and on * interstitial sites and their corresponding site balance, [L], based on Langmuirian formalisms.

Table 2
Kinetic and thermodynamic parameters for the rate equations for thiophene conversion on Ru, Pt, Re, and ReS_x, from regression of kinetic data to the functional form of the rate expressions[a].

Thermodynamic/ kinetic parameters[a]	Catalyst (mean particle size, nm; temperature, K)			
	Ru (1.6; 623)	Pt (4.8; 573)	Re (6.9; 573)	ReS_x (n/a[b], 573)
$\alpha_{measured} = k_0K_{H2}K_TK_{MHT}(1-\theta_{S'})$ (mol g-atom^{-1} s^{-1} kPa^{-2})	2.3 (±0.2) × 10^{-5}	1.8 (±1.0) × 10^{-4}	–	–
$\alpha'_{measured} = k_0K_{H2}^{0.5}K_T(1-\theta_{S'})$ (mol g-atom^{-1} s^{-1} kPa$^{-1.5}$)	–	–	2.5 (±0.3) × 10^{-6}	2.4 (±0.5) × 10^{-4}
$\beta = K_{H2}^{0.5}$ (kPa$^{-0.5}$)	–	1.3 (±0.9) × 10^{-2}	–	–
$\gamma = K_T$ (kPa^{-1})	1.1 (±0.2) × 10^{-1}	1.2 (±0.3) × 10^{-1}	7.0 (±1.1) × 10^{-2}	1.6 (±0.2) × 10^{-1}
$\eta = K_SK_{HS}K_{H2S}K_{H2}^{1}$ (unitless)	2.9 (±0.3) × 10^{2}	4.0 (±1.2) × 10^{3}	1.0 (±0.3) × 10^{3}	2.6 (±2.7) × 10^{2}

Uncertainty ranges (±) in reported values reflect 95 % confidence level.
[a] Parameters from rate equations for Ru (Eq. (11)), Pt (Eq. (12)), and Re/ReS_x (Eq. (13)).
[b] Layered structures.

pressures, observed at low conversion, was used as evidence for $H^{\delta+}$ species involved in the formation of dihydrothiophene and tetrahydrothiophene (hydrogenation path) [8,9], because such species would become more abundant as H_2S pressures increase (Step 2.2; Scheme 2). In fact, these higher THT/C_4 ratios reflect lesser contributions from secondary reactions as rates decrease with increasing H_2S, leading to concomitantly lower conversion (Section 3.2). This study shows that relative rates of formation of THT, butenes ($C_4^=$), and n-butane (C_4^0) depend only on the extent of conversion at all thiophene pressures (1−10 kPa) and H_2S/H_2 ratios ((3.3–50) × 10^{-4} and (1.5–15) × 10^{-4}) on Ru (Fig. 10) and Pt (Fig. 11). Such a natural consequence of the lower prevalent conversions renders assumptions about charged H-species unnecessary to account for these selectivity trends. In fact, selectivities at each conversion that do not depend on thiophene pressures or H_2S/H_2 ratios conclusively show that THT and C_4 products form on sites that sense the relative coverages of bound species to the same extent (i.e. on the same surface sites).

Measured thiophene conversion rates are proportional to H_2 pressure (Figs. 5 and 6) at each thiophene pressure and H_2S/H_2 ratio on Ru/SiO_2, indicating that species that depend on H_2 pressure (i.e., H*) or on H_2S pressure alone are present at much lower coverages than T* and S* species, leading to the simplified rate equation:

$$\frac{r_{Ru}}{[L]} = \frac{k_0K_{H2}K_TK_{MHT}(H_2)(T)}{\left(1 + K_T(T) + K_SK_{HS}K_{H2S}K_{H2}^{-1}\cdot(H_2S)/(H_2)\right)^2} \quad (11)$$

The regression of all rate data to the functional form of Eq. (11) led to the rate and equilibrium constants shown in Table 2 and to accurate descriptions of measured rates (Fig. 12). The relevance of each denominator term was probed using sensitivity analysis methods that showed > two-fold changes in residual errors upon ±20 % changes in the parameters in Eq. (11) (SI, S.3).

In contrast, thiophene conversion rates increased sub-linearly with H_2 pressure on Pt/SiO_2 (Fig. 9), indicative of detectable coverages of bound species containing H_2-derived H-atoms. Statistical analysis methods (SI, S.3) show that these are H* species (Step 1.1; Scheme 1),

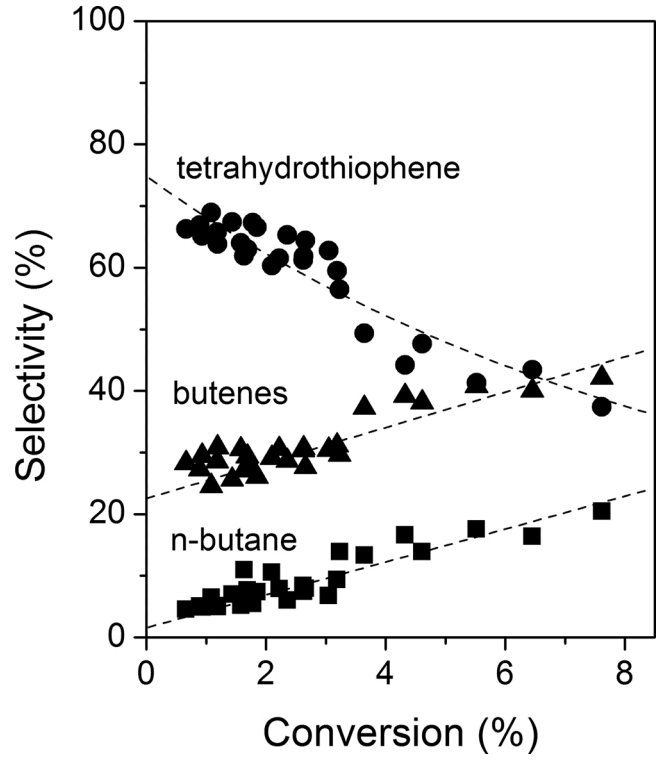

Fig. 10. Selectivity to tetrahydrothiophene (●), butenes (▲), and butane (■) as a function of thiophene conversion on Ru/SiO_2 (623 K) (3.0 MPa H_2; 1.0−10 kPa thiophene; (3.3–50.) × 10^{-4} inlet H_2S/H_2 ratio). Dashed lines indicate trends.

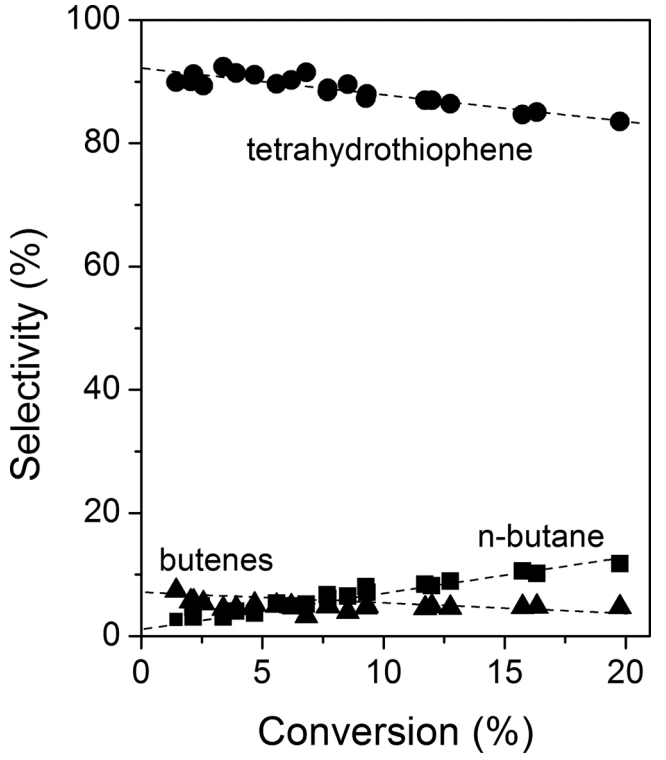

Fig. 11. Selectivity to tetrahydrothiophene (●), butenes (▲), and butane (■) as a function of thiophene conversion on Pt/SiO_2 (573 K) (2.0 MPa H_2; 1.0–10 kPa thiophene; (1.5–15) ×10^{-4} inlet H_2S/H_2 ratio). Dashed lines indicate trends.

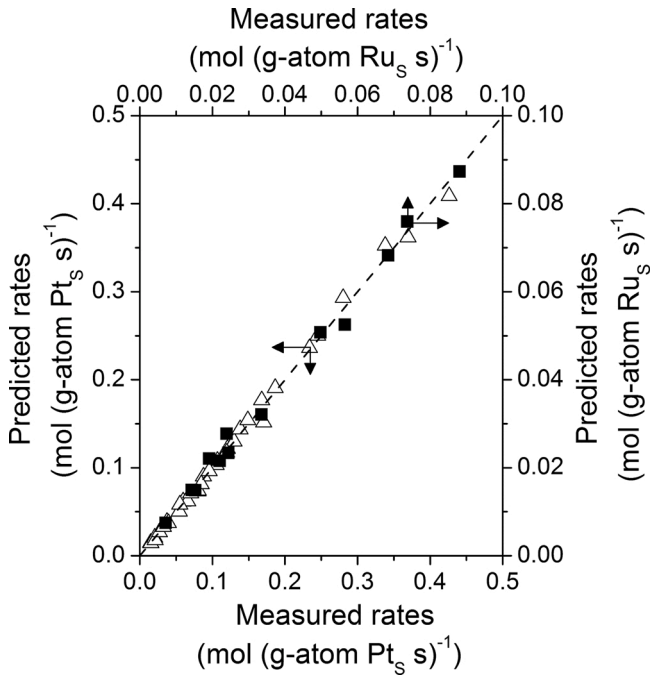

Fig. 12. Parity plot of measured rates and predicted rates from the rate expression for thiophene conversion on Pt/SiO_2 (Eq. (12)) at 573 K (△) and on Ru/SiO_2 (Eq. (11)) at 623 K (■) for a range of thiophene (1–10 kPa), H_2 (1–3 MPa) and inlet H_2S (0.2–15 kPa) pressures. The dashed line shown has a slope of unity.

leading to the rate equation:

$$\frac{r_{Pt}}{[L]} = \frac{k_0 K_{H2} K_T K_{MHT} (H_2)(T)}{\left(1 + K_{H2}^{0.5}(H_2)^{0.5} + K_T(T) + K_S K_{HS} K_{H2S} K_{H2}^{-1} \cdot (H_2S)/(H_2)\right)^2} \quad (12)$$

The regression of thiophene conversion rates on Pt (Figs. 8 and 9) to the functional form of Eq. (12) gave values for rate and equilibrium constants (Table 2) that accurately describe measured rates (Fig. 12) with regression errors that are sensitive to the magnitude of these parameters (SI, S.3), but not to those corresponding to other bound H_2S-derived species (H_2S*, HS*).

These rate equations (Eqs. (11) and (12)) identify the kinetically-detectable bound species and the stoichiometry of the rate-limiting transition state and the respective parameters that reflect their binding and free energy of formation (Section 3.6). Statistical model discrimination analyses (SI, S.4) indicate that unoccupied sites (*) are kinetically-detectable (i.e., the "1" term is measurable in the denominator), which is confirmed by a lack of significant covariance in the regression errors between the regressed numerator and denominator parameters (SI, S.5). The prevalence of these vacant sites implies that these interstitial spaces are indeed passivated and consequently stabilize reactants, intermediates, and transition states less strongly than the bare surfaces that form such S′ adlayers. For example, the relatively small or even undetectable K_{H2} values (Pt: 1.7×10^{-4} kPa^{-1}; Ru: undetectable; Table 2) contrast with those measured on sulfur-free Pt [49] (K_{H2} = 10–20 kPa^{-1}; 573 K, 3–10 nm mean diameter) and Ru [50] (K_{H2} = 20–250 kPa^{-1}; 623 K, 15 nm mean diameter) nanoparticle surfaces at 0.6–0.8 H* coverage, indicative of the much weaker H* binding on the surfaces within these refractory S′ templates.

Thiophene conversion rates on Re and ReS_x [15] are accurately

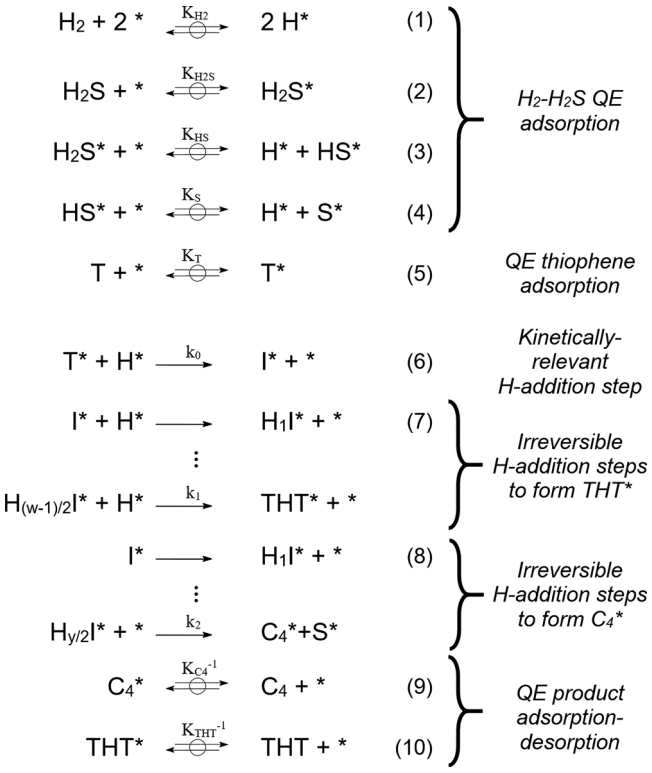

Scheme 3. Elementary steps for thiophene conversion and desulfurization-hydrogenation pathways on Re and ReS_x, adapted from [15]. Reactant and product desorption occur on *, the interstices within refractory surface templates of S adatoms, on Re and ReS_x. Adsorbed species are bound on * and include hydrogen (H*), hydrogen sulfide (H_2S*), sulfhydryl (HS*), sulfur (S*), and thiophene (T*), which form via quasi-equilibrated adsorption/desorption steps. Thiophene consumption is mediated by the addition of H* to T* (Step 6), which forms an intermediate (I*) common to both the formation of tetrahydrothiophene (THT) and butene/butane (C_4) products, via subsequent surface reactions (Steps 7 and 8) and desorption (Steps 9 and 10).

described by the rate equation:

$$\frac{r_{Re.\ ReSx}}{[L]} = \frac{k_0 K_{H2}^{0.5} K_T (H_2)^{0.5} (T)}{\left(1 + K_T(T) + K_S K_{HS} K_{H2S} K_{H2}^{-1} \cdot (H_2S)/(H_2)\right)^2} \quad (13)$$

The regressed values of each parameter are listed in Table 2. This equation differs from those on Ru and Pt in its $(H_2)^{0.5}$ numerator term (instead of $(H_2)^{1.0}$), indicating that the first H-addition to T* (Step 3.6; Scheme 3), a step that is quasi-equilibrated on Ru and Pt (Step 1.6; Scheme 1), is the kinetically-relevant step on Re and ReS_x catalysts. Eq. (13) describes rates on Re and ReS_x nanoparticles with similar binding constants for T* and S* (K_T and $K_S K_{HS} K_{H2S} K_{H2}^{-1}$; Table 2); their rate constants ($k_0 K_{H2}^{0.5} K_T (1-\theta_{S'})$, Table 2), however, are ~100-fold larger on ReS_x than on Re nanoparticles (2.4×10^{-4} mol (g-atom total Re)$^{-1}$ s^{-1} kPa$^{-1.5}$ vs. 2.5×10^{-6} mol (g-atom surface Re)$^{-1}$ s^{-1} kPa$^{-1.5}$, respectively; Table 2). Such observations reflect the combined effects of any differences in the free energies of the kinetically-relevant transition state and in the concentration of sufficiently sized ensembles, composed of $(1-\theta_{S'})$ number of interstitial sites Eq. (9), that are active during reaction on Re and ReS_x.

pressures (at any given thiophene conversion; Fig. 13) indicate that the transition state mediating THT formation steps contains a larger number of H-atoms than for C_4 formation (w > y).

These primary THT products are consumed to form C_4 at rates given by:

$$r_3 = k_3'(H^*)^z \cdot \frac{(THT^*)}{[L]} = k_3 (H_2)^{\frac{z}{2}} (THT) \cdot \frac{(^*)^2}{[L]} \quad (16)$$

where *z* is the number of H-atoms added to a bound THT* that forms the transition state that mediates THT desulfurization. With I* concentrations set by pseudo-steady state concentrations (SI, S.6), these formation rates can describe THT selectivity (defined as moles of THT formed per mole of thiophene converted), as a function of thiophene conversion:

The regression of the selectivity data in Figs. 10 and 11 to the functional form of Eq. (17):

$$S_{THT} = \frac{k_1 (H_2)^{\frac{w}{2}}}{k_1 (H_2)^{\frac{w}{2}} + k_2 (H_2)^{\frac{y}{2}}} \cdot \left(\frac{k_3 (H_2)^{\frac{z}{2}}}{k_0 K_{H2} (H_2) K_T K_{MHT}} - 1 \right)^{-1} \cdot \left\{ (1-X) - (1-X)^{\frac{k_3 (H_2)^{\frac{z}{2}}}{k_0 K_{H2} (H_2) K_T K_{MHT}}} \right\} \cdot X^{-1} \quad (17)$$

3.4. Primary thiophene-H_2 reactions on Ru and Pt catalysts

Tetrahydrothiophene (THT), butene regioisomers ($C_4^=$), and n-butane (C_4^0) are the predominant products formed in reactions of thiophene with H_2 on Ru and Pt nanoparticles [8,9] and the only products detected on Re catalysts [15]; butadiene and dihydrothiophene (<5 % selectivity) were also detected on Ru and Pt, respectively, at low conversions and low H_2 pressures, but formed $C_4^=/C_4^0$ and THT via secondary hydrogenation reactions with increasing residence time [8,9]. Butadiene and dihydrothiophene species are lumped with $C_4^=$ and THT (Figs. 10 and 11), respectively, when present, because they reflect intermediates along desulfurization and hydrogenation paths, respectively. The secondary nature of THT conversion to C_4 products is evident from THT selectivities that decrease with increasing bed residence time. Such secondary THT reactions are more prevalent on Ru (Fig. 10) than on Pt (Fig. 11) nanoparticles, as shown by the stronger effects of bed residence on THT selectivity for Ru than Pt catalysts.

The equations describing the formation rates of THT (r_1) and C_4 (r_2) via primary routes can be derived from the elementary steps in Scheme 1 (Steps 1.8 and 1.9, respectively) as:

$$r_1 = k_1'(H^*)^w \cdot \frac{(I^*)}{[L]} = k_1 (H_2)^{\frac{w}{2}} (^*) \cdot \frac{(I^*)}{[L]} \quad (14)$$

$$r_2 = k_2'(H^*)^y \cdot \frac{(I^*)}{[L]} = k_2 (H_2)^{\frac{y}{2}} (^*) \cdot \frac{(I^*)}{[L]} \quad (15)$$

where *w* and *y* are integers that reflect the number of H-atoms (proportional to $(H_2)^{0.5}$, Step 1.1; Scheme 1), added to the common intermediate (I*) that forms the transition states that mediate THT and C_4 formation. These equations reflect the bimolecular reaction of H* and I*-derived bound species, whose rates depend on the concentration of bound H-atoms (i.e., (H*)) and the probability that such species are vicinal to bound I* (i.e., (I*)/[L]). The higher THT/C_4 ratios at higher H_2

$$S_{THT} = \frac{\boldsymbol{a}}{(\boldsymbol{b}-1)} \cdot \frac{\left\{ (1-X) - (1-X)^{\boldsymbol{b}} \right\}}{X} \quad (18)$$

leads to values of **a** and **b** that are reflected in the rate ratios:

$$\frac{r_1}{r_2} = \frac{\boldsymbol{a}}{\boldsymbol{a}-1} = \frac{k_1}{k_2} \cdot (H_2)^{(w-y)/2} \quad (19)$$

$$\frac{r}{r_3} = \boldsymbol{b}^{-1} = \frac{k_0 K_{H_2} K_T K_{MHT}}{k_3} \cdot (H_2)^{1-(z/2)} \quad (20)$$

for THT (r_1) to C_4 (r_2) formation and for total thiophene conversion (r) to secondary THT conversion (r_3).

Primary selectivities were previously determined by extrapolating THT selectivities to zero conversion [8,9] using a linear version of Eq. (17) at low conversions:

$$S_{THT} = \frac{k_1 (H_2)^{\frac{w}{2}}}{k_1 (H_2)^{\frac{w}{2}} + k_2 (H_2)^{\frac{y}{2}}} \left(1 - \frac{k_3 (H_2)^{\frac{z}{2}}}{k_0 K_{H2} (H_2) K_T K_{MHT}} \cdot \frac{X}{2} \right) = \boldsymbol{a} \cdot \left(1 - \frac{\boldsymbol{b}}{2} \cdot X \right) \quad (21)$$

which is accurate for (**b** X) values much smaller than unity. Such criteria are met at low conversions when secondary THT reactions are much slower than thiophene conversion ($k_3 (H_2)^{z/2} < k_0 K_{H2} (H_2) K_T K_{MHT}$). These criteria are met on Pt/SiO_2 (for which selectivity changes from 91 % to 84 % between 2 and 20 % conversion; Fig. 11), but not on Ru/SiO_2 (for which selectivity changes from 62 % to 38 % between 2 and 8 % conversion; Fig. 10). Thus, THT selectivity data on Ru/SiO_2 require that regressions use Eq. (18) (instead of Eq. (21)).

The regression of all selectivity data on Ru and Pt (Figs. 10 and 11), measured at each H_2 pressure, to the functional forms of Eqs. (18) and

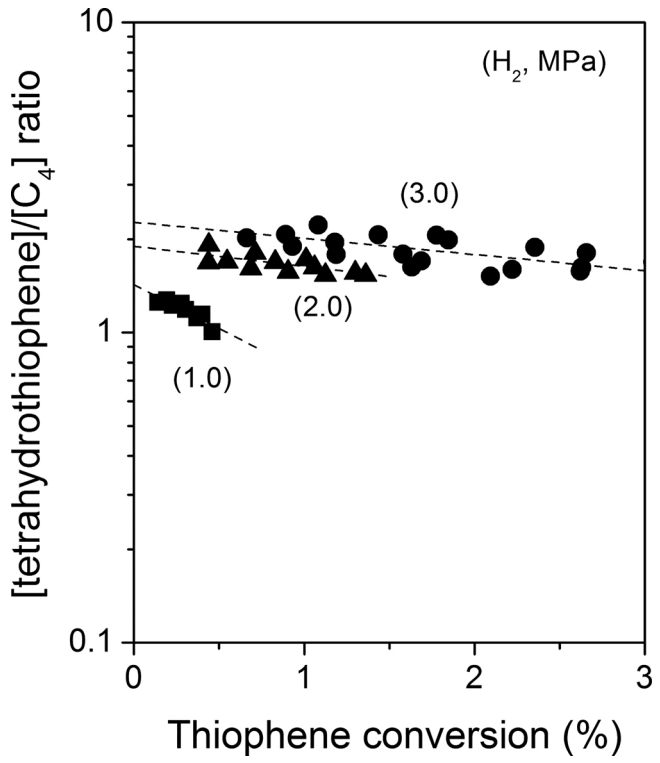

Fig. 13. Tetrahydrothiophene to butene/butane (C_4) molar ratios as a function of thiophene conversion at 3.0 MPa (●), 2.0 MPa (▲), and 1.0 MPa (■) H_2 pressures over a range of thiophene (1−10 kPa) and inlet H_2S/H_2 ratios ((3.3–100) × 10^{-4}) at 623 K on Ru/SiO_2. Dashed lines indicate trends.

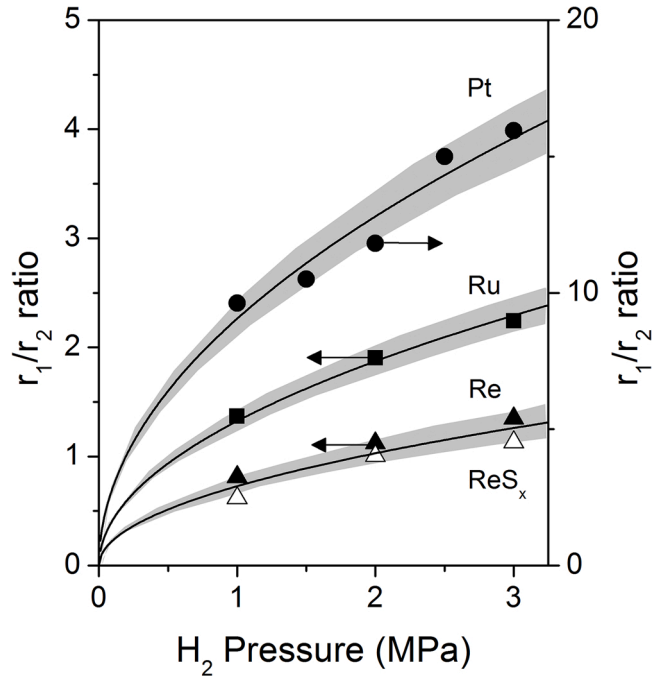

Fig. 14. Ratio of primary THT (r_1) to C_4 (r_2) formation rates (Eq. (19)) from parameters regressed from selectivity data to the functional form of Eq. (18) for Ru/SiO_2 at 623 K (■) and Eq. (21) for Pt/SiO_2 at 573 K (●); ratios for Re (▲) and ReS_x (△) at 573 K are also reported (adapted from [15]). Curves reflect the regression of r_1/r_2 to ~$(H_2)^{0.5}$ ((w–y)/2 = 0.5; Eq. (19)). Lightly shaded regions reflect 95 % confidence intervals of the fitted parameter estimates obtained from the regression.

(21), respectively, provides a value for **a**, and consequently a value for r_1/r_2 (through Eq. (19)), at a given H_2 pressure. These ratios (r_1/r_2) show a $(H_2)^{0.5}$ dependence (Fig. 14) on Ru and Pt (i.e., (w–y)/2 = 0.5, Eq. (19)), consistent with similar THT formation transition states that contain one more H-atom than for C—S bond activation to form C_4, as also found on Re-based catalysts [15].

On all catalysts, THT/C_4 ratios show the same dependence on H_2 pressure, but these ratios (at any given H_2 pressure) are larger on Pt than on Re or ReS_x, with Ru showing intermediate values (Fig. 14). These trends reflect transition state structures for THT and C_4 formations that differ by one H-atom on all catalysts and also relative stabilities of these two transition states that seem to depend on catalyst identity. The differences in the relative extents to which THT and C_4 formation transition states are stabilized on these catalysts are evident from their different k_1/k_2 values (i.e., 0.023 ± 0.002 $kPa^{-0.5}$ for Re and ReS_x; 0.045 ± 0.006 $kPa^{-0.5}$ for Ru; 0.27 ± 0.04 $kPa^{-0.5}$ for Pt, Eq. (19)). These working surfaces also stabilize transition states responsible for $C_4^=$ hydrogenation to different extents, as evident from the higher $C_4^0/C_4^=$ ratios on Pt than on Ru (Fig. S.7-1; SI, S.7); these $C_4^0/C_4^=$ ratios (<2.5) remain far from equilibrium (10^5–10^6 at 1−3 MPa H_2, 573−623 K), in contrast with their equilibrated interconversions on bare Ru and Pt metal surfaces [20], indicative of the passivated nature of these S′-covered surfaces. These observations imply that active interstices differ in their binding of transition states on Ru, Pt, and Re surfaces, as discussed in Section 3.6.

3.5. Secondary THT desulfurization reactions on Ru and Pt catalysts

The effects of H_2 pressure on secondary THT desulfurization rates (Eq. (16)) were examined from the consequences of residence time on selectivity using formalisms based on Eqs. (18) or (21). The r/r_3 ratios defined in Eq. (20) increased with increasing H_2 pressure (Fig. 15) with functional dependences of $(H_2)^{1.5}$ and $(H_2)^1$ on Ru and Pt, respectively (Fig. 15); these trends correspond to z values of −1 and 0 (in Eq. (20)),

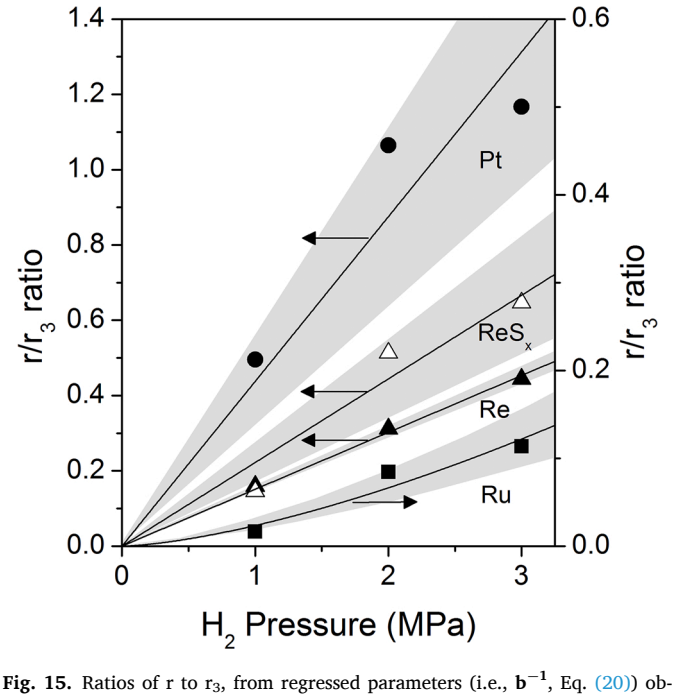

Fig. 15. Ratios of r to r_3, from regressed parameters (i.e., $\mathbf{b}^{-1}$, Eq. (20)) obtained by regressing selectivity data to the functional form of Eq. (18) for Ru/SiO_2 (■) at 623 K and to the functional form of Eq. (21) for Pt/SiO_2 (●) at 573 K; ratios for Re (▲) and ReS_x (△) at 573 K are also reported (adapted from [15]). Curves represent the regression of r/r_3 to ~$(H_2)^{1.0}$ for Pt, Re, and ReS_x and to ~$(H_2)^{1.5}$ for Ru. Lightly shaded regions reflect 95 % confidence intervals of the fitted parameter estimates obtained from the regression.

	Elementary Step	If equilibrated …	If kinetically-relevant…
(1)	$THT + * \overset{k_A}{\underset{k_{-A}}{\rightleftharpoons}} THT*$	$(THT*) = K_A(THT)\cdot(*)$ $K_A = \frac{k_A}{k_{-A}}$	$r_3 = k_A(THT)(*)$
(2)	$THT* + * \overset{k_B}{\underset{k_{-B}}{\rightleftharpoons}} TrHT* + H*$	$(TrHT*) = \frac{K_B K_A (THT)}{K_{H2}^{0.5}(H_2)^{0.5}}\cdot(*)$ $K_B = \frac{k_B}{k_{-B}}$	$r_3 = k_B K_A (THT)(*)$
(3)	$TrHT + * \overset{k_C}{\underset{k_{-C}}{\rightleftharpoons}} DHT* + H*$	$(DHT*) = \frac{K_C K_B K_A (THT)}{K_{H2}(H_2)}\cdot(*)$ $K_C = \frac{k_C}{k_{-C}}$	$r_3 = \frac{k_C K_B K_A}{K_{H2}^{0.5}}\cdot\frac{(THT)}{(H_2)^{0.5}}(*)$
(4)	$DHT* + * \overset{k_D}{\underset{k_{-D}}{\rightleftharpoons}} MHT* + H*$	$(MHT*) = \frac{K_D K_C K_B K_A (THT)}{K_{H2}^{1.5}(H_2)^{1.5}}\cdot(*)$ $K_D = \frac{k_D}{k_{-D}}$	$r_3 = \frac{k_D K_C K_B K_A}{K_{H2}}\cdot\frac{(THT)}{(H_2)}(*)$
(5)	$H_2 + 2* \overset{K_{H2}}{\rightleftharpoons} 2H*$	$(H*) = K_{H_2}^{0.5}(H_2)^{0.5}\cdot(*)$	--

Scheme 4. Elementary steps of tetrahydrothiophene adsorption and surface dehydrogenation.

which indicate that transition states that mediate THT desulfurization contain similar or fewer H-atoms than THT molecules. Therefore, they require H-removal from THT to form the transition state that mediates THT desulfurization.

THT dehydrogenation steps can be represented by steps (Scheme 4) that form bound trihydrothiophene (TrHT*), dihydrothiophene (DHT*), and monohydrothiophene (MHT*) intermediates via stepwise H-removal from THT. The H_2 pressure effects on r_3 ($\sim(H_2)^{z/2}$) serve to identify the kinetically-relevant step that forms I_{CS}*, the intermediate that is also involved in C—S scission from THT. THT desulfurization rates (r_3) involve H-abstraction from TrHT* (Step 4.3; Scheme 4) on Ru and either H-abstraction from THT* (Step 4.2; Scheme 4) or THT adsorption (Step 4.1; Scheme 4) on Pt, as kinetically-relevant steps. These I_{CS}* species consist of intermediates derived via partial thiophene hydrogenation (Scheme 4), which contain fewer H-atoms than THT but more than thiophene, as also observed on Re and ReS_x [15].

The molecularity of the C—S bond scission transition state, formed from thiophene by H-addition or from THT by H-removal, reflects that of a partially-hydrogenated bound thiophene molecule; it is formed from a specific surface intermediate (I_{CS}*), which can be inferred from counting the number of H-atoms added to thiophene (based on kinetic data; Figs. 6 and 9) and the number of H-atoms removed from THT (based on information from measured selectivity data; Fig. 15) to form the kinetically-relevant transition state that mediates primary and secondary desulfurization, respectively. I_{CS}* forms after the kinetically-relevant step for thiophene conversion (the addition of H* to MHT*,

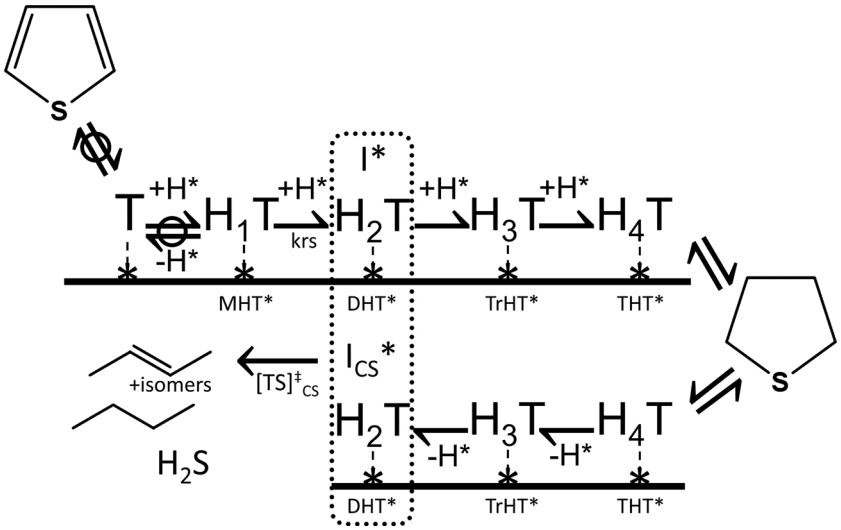

Scheme 5. Primary and secondary reactions on active interstitial sites (*), retained on refractory surface templates of S adatoms formed on Ru and Pt. Equilibrated H* addition to bound thiophene species (T*) forms monohydrothiophene species (MHT*), which subsequently undergo kinetically-relevant H* addition, which controls the rate of thiophene conversion to form a common surface intermediate, I*. I* intermediates undergo surface reactions to form the transition states that mediate tetrahydrothiophene (THT) and butene/butane ($C_4^=$, C_4^0) formation. Readsorption of THT on (similar) surfaces can form secondary $C_4^=$ and C_4^0 products through sequential dehydrogenation steps and formation of the intermediate (I_{CS}*), which contains more H-atoms than thiophene but fewer H-atoms than THT, that subsequently forms the C—S bond scission transition state, $[TS]^{\ddagger}_{CS}$.

Step 1.7; Scheme 1); thus I_{CS}* contains more H-atoms than MHT* (e.g., DHT*, TrHT*, THT*). H_2 pressure effects on primary THT/C_4 ratios (r_1/r_2; Fig. 14) show that transition states that mediate THT formation and C—S bond scission differ by one H-atom ($r_1/r_2 \sim (H_2)^{0.5}$, Eq. (19)); thus THT formation rates are limited by one H* addition to I_{CS}*.

THT desulfurization rates depend on $(H_2)^{-0.5}$ (z = −1; Eq. (16)) on Ru (Fig. 15), indicating that TrHT*-THT* interconversions are quasi-equilibrated on these surfaces (Step 4.2; Scheme 4), and in equilibrium with gaseous THT and H_2 (Steps 4.1 and 4.5; Scheme 4). Such a H_2 dependence presents two possibilities for the identity of I_{CS}*: either it is TrHT* itself or I_{CS}* is formed after kinetically-relevant H-removal from TrHT*, as both are consistent with secondary desulfurization rates that depend on $\sim(THT)(H_2)^{-0.5}$. In the first scenario, the same molecularity would persist between the structure of the C—S bond scission transition state and TrHT*, and C—S bond scission rates would depend on the concentration of these bound TrHT intermediates, which is set by H_2 pressure as a consequence of its equilibrium with bound THT, H_2 (g), and THT(g). The relative formation of THT over C_4 would increase with H_2 pressure, in a manner consistent with the $\sim(H_2)^{0.5}$ dependence observed for r_1/r_2 (Eq. (19)). THT/C_4 ratios, however, do not remain constant at a given H_2 pressure, as required if TrHT* were to form the C—S bond scission transition state; instead these THT/C_4 ratios decrease significantly (Fig. 13) with increasing thiophene (1−10 kPa) conversion (e.g., 1–3 %) at a given excess H_2 pressure condition (1−3 MPa). Such behaviors indicate that TrHT* cannot be the immediate precursor to forming the transition state that mediates C—S bond cleavage and that, instead, the formation of I_{CS}* must be mediated by the kinetically-relevant removal of H-atom from TrHT* (Step 4.3; Scheme 4). Thus, DHT* remains the only plausible structure for I_{CS}* (Scheme 5), which contains more H-atoms than MHT*, which is in equilibrium with gaseous thiophene and H_2, and fewer H-atoms than TrHT*, which is in equilibrium with gaseous THT and H_2.

A similar analysis can be applied to interrogate the identity of I_{CS}* on Pt surfaces. In contrast to Ru, secondary desulfurization rates on Pt do not depend on H_2, which suggests either THT* is I_{CS}* or that kinetically-relevant H-removal from THT* leads to the (re)formation of I_{CS}* on the surface. C—S bond scission transition states that form from THT* is inconsistent with primary THT/C_4 formation rate ratios (r_1/r_2; Eq. (19)) that depend on $\sim(H_2)^{0.5}$ (Fig. 14). Thus, I_{CS}* is formed after a kinetically-relevant (H-abstraction) step from THT* and consequently contains fewer H-atoms than THT* (e.g., DHT* and TrHT*). Any subsequent H-removal steps from TrHT* are kinetically silent and thus, a more precise identification of I_{CS}* is not experimentally accessible; both DHT* and TrHT* could plausibly form the C—S bond transition state and also form the THT formation transition state upon H* addition, in a manner consistent with the $(H_2)^{0.5}$ dependence observed for primary THT/C_4 formation rate ratios.

On all refractory S′ templates (Ru, Pt, Re), a partially-hydrogenated thiophene (I_{CS}*) acts as the immediate precursor to C—S cleavage transition states. THT forms as a consequence of an "overhydrogenation mistake" of I_{CS}*; this mistake can be corrected by readsorption, dehydrogenation, and C—S bond cleavage via secondary reactions that become more prevalent with increasing bed residence time. The involvement of these partially-hydrogenated precursors (I_{CS}*) before C—S bonds can be cleaved is also found for C—C and C—O bond activation in hydrogenolysis of alkanes [18–21] and alkanols [51] on metal surfaces; the high activation barriers required for C—C and C—O cleavage, caused in part by the preceding sequence of endothermic C—H activation steps, are compensated by entropy gains upon formation of gaseous H_2 molecules. These dehydrogenation events of saturated reactants weaken C—C/C—O bonds through the formation of multiple bonds between the C and/or O atoms and surfaces (C/O—M); the resulting electron back donation from surfaces into C—C/C—O antibonding orbitals allows the more facile cleavage of such bonds. Similarly, the partial dehydrogenation of THT is required to recover the I_{CS}* species that cleaves the C—S bond. These mechanistic conclusions for C—S bond activation reactions illustrate the general requirement for removal of H-atoms in order to cleave strong C—X bonds (C—S bonds here).

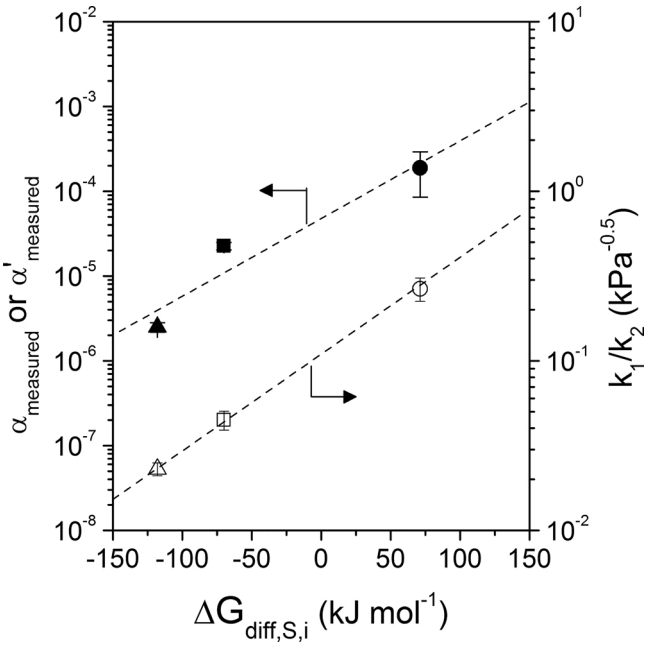

Fig. 16. Regressed rate constant, $\alpha_{measured}$ ($k_0K_{H2}K_TK_{MHT}(1-\theta_{S'})$; Table 2, units of mol thiophene (g-atom s $kPa^2)^{-1}$) and $\alpha'_{measured}$ ($k_0K_{H2}^{0.5}K_T(1-\theta_{S'})$; Table 2, units of mol thiophene (g-atom s $kPa^{1.5})^{-1}$) for Pt (●) at 573 K, Ru (■) at 623 K, and Re (▲) at 573 K and the ratio of rate constants k_1/k_2 (Eq. (22)) for primary THT to primary C_4 formation on Pt (○) at 573 K, Ru (□) at 623 K, and Re (△) at 573 K as a function of S adatom formation free energy ($\Delta G_{diff,S,i}$) to form S* and gaseous H_2 (Eq. (4)), at 4/9 ML coverage of S, calculated using density functional theory (Table S.1-3) on 3 × 3 close-packed surfaces. Error bars reflect uncertainty ranges at 95 % confidence level. Dashed lines indicate trends.

Table 3
M–S binding energy at 4/9 ML S adlayer coverage from density functional theory (DFT).

metal (crystal facet)	H_2S/H_2 [a]	½ S_2 [b]	S· [c]
Re (0001)	−145	−219	−515
Ru (0001)	−100	−174	−470
Pt (111)	+42	−32	−328

[a,b,c] Defined as the potential energy of forming an S adatom through: a) $H_2S + * \rightarrow S^* + H_2$; b) ½ $S_2 + * \rightarrow S^*$; c) S(radical) + * → S*.

3.6. Consequences of M—S bond energy on the concentration of active interstices within refractory templates of strongly-bound S adatoms, measured rates, and THT/C_4 selectivities

Thiophene conversion turnover rates on Ru [8], Pt [9], and Re [15] nanoparticles differ by nearly 100-fold when rates are normalized by the total number of surface metal atoms in the fresh nanoparticles, a reporting protocol that ensures replication among different studies. The resulting turnover rates, however, do not reflect the intrinsic reactivity of the working surfaces, because the number of exposed surface atoms do not directly represent the number and size of the active interstices that the [L] term denotes in the Langmuirian treatments used here to assess the mechanistic basis for measured rates (Eq. 2.15; Scheme 2). The fraction of the total surface (θ_L) that is not covered by irreversibly bound S adatoms depends on the identity and binding properties of the

underlying nanoparticle surfaces; they determine the number and nature of the interstices available for reversible S* binding and for stabilizing the requisite transition states, thus meeting the requirements for catalytic desulfurization turnovers.

The fraction of the surface composed of interstices can be inferred from the theoretical treatments in Section 3.1, which indicate that refractory S adatoms (S′) bind strongly to these surfaces until S–S repulsion prevents additional adsorption (Fig. 2); the coverages of these irreversibly bound S′ ($\theta_{S'}$) are reached at approximately 2/3 ML, 1/2 ML, and 1/3 ML for Re(0001), Ru(0001), and Pt(111). Comparisons among different catalyst compositions must account for such differences in the concentration of these interstitial ensembles that remain available for reversible binding, as well as for differences in the reactivity of such spaces, which is also dictated by the identity of the metal in the underlying substrate.

The reactivity of catalytic materials in the desulfurization of organosulfur compounds has been linked heuristically, but seldom quantitatively, to the strength of M—S bonds in solids [5,7,13], which are decidedly influential for the binding of reactants and transition states, but which more relevantly determine the prevalence and binding properties of interstitial spaces within refractory S′ adlayers. The magnitude of the lumped parameter $\alpha_{measured}$ (or $\alpha'_{measured}$) increases monotonically with the free energy of formation of S adatoms ($\Delta G_{diff,S,i}$) at 4/9 ML coverage as determined by DFT (Fig. 16). These $\alpha_{measured}$ (or $\alpha'_{measured}$) values, however, do not only reflect free energy differences between the relevant transition state and its gas phase precursors but also include differences in the concentration of accessible interstices on which turnovers occur (Eq. (10)). DFT calculations (Section 3.1) indicate, however, the fraction of exposed atoms that remain free of S′ on Pt (111) is only about twice as large as on Ru(0001) and Re(0001); these fractions become even more similar on the latter two surfaces. Thus, the number of interstitial ensembles cannot, on its own, account for the nearly 100-fold differences in measured α values among these catalysts.

These different turnover rates and α values indicate, instead, that interstitial ensembles present in the metal surfaces stabilize the kinetically-relevant C—H bond forming transition states to different extents and that they do so in ways that reflect the M—S bond strength (Table 3) as shown by α values that correlate to $\Delta G_{diff,S,i}$ values at 4/9 ML (Fig. 16). Such correlations imply that these transition states "sense" the nature of the working surfaces in a way that extends how strongly they can bind S-atoms, which remain similar for interstitial sites as different surfaces become passivated by a strongly-bound S′ adlayer when exposed to a given sulfur chemical potential (and H_2S/H_2 ratio). Instead, the different free energies of formation of these transition states reflect their spatial demands, which, in contrast to the single site needed to bind an additional S* atom, require several sites and, in turn, suggest that the configurations of S′ differ and determine the size of the ensembles retained on these different catalyst surfaces. M—S binding (at a given sulfur coverage) thus correlates with these transition state formation energies because it describes the relative space retained within these interstices, revealing that reactivity can benefit from the additional space available on more weakly-binding Pt surfaces (compared with Ru or Re surfaces). In contrast, M—S binding energies at a given coverage (e.g., 4/9 ML) are poor descriptors of S* adsorption energies ($\eta = K_S K_{HS} K_{H2S} K_{H2}^{-1}$; Table 2), perhaps counterintuitively. Instead, these measured S* adsorption energies reflect the S* atom binding at near-saturated surfaces (at coverages ($\theta_{S'}$) that depend on the catalyst identity; Section 3.1) and on some sites that may be otherwise inaccessible to transition states.

The different reactivity of the interstitial ensembles on these different catalysts is perhaps most evident when assessing the relative rates of primary THT (r_1) and C_4 (r_2) formation (Fig. 14), which occur on the same active surface for a given catalyst. These r_1/r_2 rate ratios depend similarly on $(H_2)^{0.5}$ (Eq. (19)) on all catalysts but their magnitude is larger on Pt than Ru and Re at all H_2 pressures; these ratios do not depend on the number of sites or ensembles. Consequently, they unambiguously reflect the difference in the free energies between these two transition states. The ratio of their respective rate constants (k_1/k_2; Eq. (19)) reflects differences in the effective free energies of forming each of their kinetically-relevant transition states, on each surface:

$$\frac{k_1}{k_2} = \exp\left(- \frac{\left(\Delta G^{\ddagger}_{eff,\,THT} - \Delta G^{\ddagger}_{eff,\,C4}\right)}{RT} \right) \tag{22}$$

with the difference in free energies given by:

$$\left(\Delta G^{\ddagger}_{eff,\,THT} - \Delta G^{\ddagger}_{eff,C4}\right) = G^{\ddagger}_{THT} - \frac{1}{2} G_{H2} - G^{\ddagger}_{C4} \tag{23}$$

where $G^{\ddagger}_{THT}$ and $G^{\ddagger}_{C4}$ reflect the free energies of the THT and C_4 formation transition states, respectively, and G_{H2} reflects the free energy of gaseous H_2. These k_1/k_2 ratios increase with increasing free energy of formation of S adatoms ($\Delta G_{diff,S,i}$) (Fig. 16), suggesting that the relative binding of these two transition states varies in a monotonic manner with the strength of M—S binding of each underlying substrate.

M—S bond energies reported in the literature from experiment [42–46,52] or theory [53,54] are often assessed at similar sulfur coverages and represent fortuitous descriptors of thiophene conversion rates. These M—S bond energies reflect changes in the size of the interstices, in a predictable manner, which, in turn, influences how those interstices stabilize – to different extents – the transition states that determine the rates of THT and C_4 formation. These coincidental correlations have led to their ubiquitous use and justification [5,7,13] for the purposes of relating reactivity to the strength of sulfur binding, for instance on different metal surfaces or on coordinatively-unsaturated (edge) sites. In fact, the reactivity depends solely on the interstices present within a permanent S′ template. These observations and their mechanistic underpinnings highlight the concepts and realities that are pervasive in describing reactivity on surfaces that become reactive at all only because reactant-derived refractory adlayers act to passivate them; in doing so, passivation enables the reversible binding of reactants and products that represents the defining feature of an active site or ensemble.

4. Conclusions

Under the sulfur chemical potentials prevalent in HDS practice, strongly-bound S-atoms (S′) form refractory adlayers on exposed transition metal surfaces. These permanent S′ adlayers "poison" such surfaces, severely inhibiting reactivity (e.g., hydrogenolysis, hydrogenation, reforming, etc.) even after the subsequent removal of sulfur containing molecules from reactant streams, reflecting the irreversibly-bound nature of these S′ atoms. Theory predicts, however, that these adlayers do not cover the surface completely, as a consequence of the significant S′–S′ repulsions that arise as coverages increase, leaving behind passivated, interstitial spaces that bind reactants, intermediates, and transition states reversibly, as required for catalytic turnovers. The interstitial sites that remain cannot be counted by titrant or chemisorption uptake experiments, which are performed with pretreatments and at measurement conditions far removed from those prevalent during reaction; thus, even measured turnover rates, per exposed surface atom, reflect both the number and the binding of these interstices.

These interstices bind the transition states that mediate thiophene desulfurization and hydrogenation reactions; the rates of these reactions decrease with increasing H_2S/H_2, reflecting weakly-bound S* that replace vacant interstitial sites (*), but they also respond reversibly to H_2S/H_2, reflecting the equilibrium of S* atoms with gas phase H_2S-H_2 mixtures. Such interstices, within an unreactive S′ adlayer, compose a working surface that consequently lends itself to Langmuirian treatments. These kinetic and selectivity assessments indicate that H*-addition to thiophene-derived intermediates controls the rates of thiophene

conversion to tetrahydrothiophene (THT) and butene/butane (C_4). Their selective formations are independent of thiophene pressure and H_2S/H_2 ratio, despite the prevalence of bound thiophene and S* intermediates on the surface, indicating both pathways occur on the same surfaces.

Analyses of secondary THT reactions reveal another pathway to desulfurization: C—S bond scission transition states are re-formed, upon THT readsorption and subsequent surface dehydrogenation steps, ultimately correcting the initial "overhydrogenation mistake." The precursor that forms these C—S bond cleavage transition states is more saturated than thiophene but less saturated than THT; the requisite formations of these partially-hydrogenated intermediates find precedence in those involved in C—C and C—O bond activations for (cyclo) alkane and alkanol hydrogenolysis reactions, respectively [18–21,51]. For these C—X (X = C, O, S) bond scission reactions, the bond being cleaved is weakened upon additional attachments to the surface, made possible by C—H bond cleavage steps that are compensated by the entropic gains from H_2 evolution.

Thiophene conversion rates, normalized by exposed metal atoms, differ by nearly 100-fold on Pt, Ru, and Re, reflecting the differences in the number and binding of interstitial sites among these catalysts. S′ adlayer coverages on these exposed surfaces reach 1/3 ML, 1/2 ML, and 2/3 ML on Pt(111), Ru(0001), and Re(0001), as predicted by theory, under the temperatures and H_2S/H_2 ranges employed in these studies; thus, the concentration of interstitial spaces retained by these surfaces cannot alone account for these measured rate differences. These different rates reflect instead the differences in transition state bindings on their respective interstitial sites, which presumably bind S atoms similarly as refractory S′ adlayers form. The binding of transition state structures, however, likely requires several sites, in contrast to the single site required for adsorbing S atoms, leading to reactivity that depends on the connectivity of sites among these interstices. The rate constants measured on Pt, Ru, and Re correlate to their respective M—S binding energies, calculated at a constant sulfur coverage, and do so only because these M—S bindings describe the relative space retained within these surfaces. These correlations merely indicate that reactivity can benefit when the active interstices are composed of more interconnected ensembles (e.g., on Pt) compared to isolated sites (e.g., on Re), which must bind the spatially demanding transition states. The ubiquitous use of M—S bindings as a descriptor of HDS reactivity then seems, at best, phenomenological, motivated by their fortuitous, monotonic trends with rates of reactions that occur, instead, on passivated spaces that bind adsorbates and transition states much more weakly than the underlying substrate.

Declaration of Competing Interest

The authors declare that they have no known competing financial interests or personal relationships that could have appeared to influence the work reported in this paper.

Acknowledgements

We acknowledge the financial support for this research from the Director, Office of Basic Energy Sciences, Chemical Sciences Division of the U.S. Department of Energy.

Appendix A. Supplementary data

Supplementary material related to this article can be found, in the online version, at doi:https://doi.org/10.1016/j.apcatb.2020.119797.

References

[1] J.V. Lauritsen, J. Kibsgaard, G.H. Olesen, P.G. Moses, B. Hinnemann, S. Helveg, J. K. Nørskov, B.S. Clausen, H. Topsøe, E. Lægsgaard, et al., J. Catal. 249 (2007) 220, https://doi.org/10.1016/j.jcat.2007.04.013.
[2] A. Borgna, E.J.M. Hensen, J.A.R. van Veen, J.W. Niemantsverdriet, J. Catal. 221 (2004) 541, https://doi.org/10.1016/j.jcat.2003.09.018.
[3] F. Cesano, S. Bertarione, A. Piovano, G. Agostini, M.M. Rahman, E. Groppo, F. Bonino, D. Scarano, C. Lamberti, S. Bordiga, et al., Catal. Sci. Technol. 1 (2011) 123, https://doi.org/10.1039/c0cy00050g.
[4] R. Prins, V.H.J. de Beer, G.A. Somorjai, Catal. Rev. 31 (1989) 1, https://doi.org/10.1080/01614948909351347.
[5] T.A. Pecoraro, R.R. Chianelli, J. Catal. 67 (1981) 430, https://doi.org/10.1016/0021-9517(81)90303-1.
[6] A. Niquille-Röthlisberger, R. Prins, J. Catal. 242 (2006) 207, https://doi.org/10.1016/j.jcat.2006.06.009.
[7] E.J.M. Hensen, H.J.A. Brans, G.M.H.J. Lardinois, V.H.J. de Beer, J.A.R. van Veen, R.A. van Santen, J. Catal. 192 (2000) 98, https://doi.org/10.1006/jcat.2000.2824.
[8] H.M. Wang, E. Iglesia, J. Catal. 273 (2010) 245, https://doi.org/10.1016/j.jcat.2010.05.019.
[9] H.M. Wang, E. Iglesia, Chemcatchem. 3 (2011) 1166, https://doi.org/10.1002/cctc.201100027.
[10] J. Quartararo, S. Mignard, S. Kasztelan, J. Catal. 192 (2000) 307, https://doi.org/10.1006/jcat.2000.2825.
[11] A. Ishihara, F. Dumeignil, J. Lee, K. Mitsuhashi, E.W. Qian, T. Kabe, Appl. Catal. A Gen. 289 (2005) 163, https://doi.org/10.1016/j.apcata.2005.04.056.
[12] J.K. Nørskov, B.S. Clausen, H. Topsøe, Catal. Lett. 13 (1992) 1, https://doi.org/10.1007/BF00770941.
[13] H. Toulhoat, P. Raybaud, J. Catal. 216 (2003) 63, https://doi.org/10.1016/s0021-9517(02)00118-5.
[14] C.J.H. Jacobsen, E. Törnqvist, H. Topsøe, Catal. Lett. 63 (1999) 179, https://doi.org/10.1023/A:1019017004845.
[15] E. Yik, E. Iglesia, J. Catal. 368 (2018) 411, https://doi.org/10.1016/j.jcat.2018.03.031.
[16] N.Y. Topsøe, H. Topsøe, J. Catal. 139 (1993) 641, https://doi.org/10.1006/jcat.1993.1056.
[17] T.I. Korányi, F. Moreau, V.V. Rozanov, E.A. Rozanova, J. Mol. Struct. 410–411 (1997) 103, https://doi.org/10.1016/S0022-2860(96)09484-7.
[18] D.W. Flaherty, D.D. Hibbitts, E.I. Gürbüz, E. Iglesia, J. Catal. 311 (2014) 350, https://doi.org/10.1016/j.jcat.2013.11.026.
[19] D.W. Flaherty, D.D. Hibbitts, E. Iglesia, J. Am. Chem. Soc. 136 (2014) 9664, https://doi.org/10.1021/ja5037429.
[20] D.W. Flaherty, E. Iglesia, J. Am. Chem. Soc. 135 (2013) 18586, https://doi.org/10.1021/ja4093743.
[21] D.W. Flaherty, A. Uzun, E. Iglesia, J. Phys. Chem. C 119 (2015) 2597, https://doi.org/10.1021/jp511688x.
[22] T.C. Ho, Q. Shen, J.M. McConnachie, C.E. Kliewer, J. Catal. 276 (2010) 114, https://doi.org/10.1016/j.jcat.2010.09.005.
[23] G. Kresse, J. Furthmüller, Phys. Rev. B 54 (1996) 11169, https://doi.org/10.1103/PhysRevB.54.11169.
[24] G. Kresse, J. Furthmüller, Comput. Mater. Sci. 6 (1996) 15, https://doi.org/10.1016/0927-0256(96)00008-0.
[25] G. Kresse, J. Hafner, Phys. Rev. B 49 (1994) 14251, https://doi.org/10.1103/PhysRevB.49.14251.
[26] G. Kresse, J. Hafner, Phys. Rev. B 47 (1993) 558, https://doi.org/10.1103/PhysRevB.47.558.
[27] P. Kravchenko, C. Plaisance, D. Hibbitts, A New Computational Interface for Catalysis (2019), https://doi.org/10.26434/chemrxiv.8040737.v3.
[28] G. Kresse, D. Joubert, Phys. Rev. B 59 (1999) 1758, https://doi.org/10.1103/PhysRevB.59.1758.
[29] P.E. Blöchl, Phys. Rev. B 50 (1994) 17953, https://doi.org/10.1103/PhysRevB.50.17953.
[30] B. Hammer, L.B. Hansen, J.K. Nørskov, Phys. Rev. B 59 (1999) 7413, https://doi.org/10.1103/PhysRevB.59.7413.
[31] J.P. Perdew, K. Burke, M. Ernzerhof, Phys. Rev. Lett. 77 (1996) 3865, https://doi.org/10.1103/PhysRevLett.77.3865.
[32] Y. Zhang, W. Yang, Phys. Rev. Lett. 80 (1998) 890, https://doi.org/10.1103/PhysRevLett.80.890.
[33] B.T. Loveless, C. Buda, M. Neurock, E. Iglesia, J. Am. Chem. Soc. 135 (2013) 6107, https://doi.org/10.1021/ja311848e.
[34] D.D. Hibbitts, B.T. Loveless, M. Neurock, E. Iglesia, Angew. Chemie Int. Ed. 52 (2013) 12273, https://doi.org/10.1002/anie.201304610.
[35] D. Hibbitts, E. Dybeck, T. Lawlor, M. Neurock, E. Iglesia, J. Catal. 337 (2016) 91, https://doi.org/10.1016/j.jcat.2016.01.010.
[36] A. Almithn, D. Hibbitts, ACS Catal. 8 (2018) 6375, https://doi.org/10.1021/acscatal.8b01114.
[37] A.S. Almithn, D.D. Hibbitts, Aiche J. 64 (2018) 3109, https://doi.org/10.1002/aic.16110.
[38] P. Kravchenko, V. Krishnan, D. Hibbitts, J. Phys. Chem. C 124 (2020) 13291, https://doi.org/10.1021/acs.jpcc.0c04024.

[39] X. Liu, R.J. Madix, C.M. Friend, Chem. Soc. Rev. 37 (2008) 2243, https://doi.org/10.1039/b800309m.
[40] H.A. Yoon, N. Materer, M. Salmeron, M.A. Van Hove, G.A. Somorjai, Surf. Sci. 376 (1997) 254, https://doi.org/10.1016/S0039-6028(96)01405-7.
[41] D.G. Kelly, A.J. Gellman, M. Salmeron, G.A. Somorjai, V. Maurice, M. Huber, J. Oudar, Surf. Sci. 204 (1988) 1, https://doi.org/10.1016/0039-6028(88)90264-6.
[42] J.G. McCarty, H. Wise, J. Chem. Phys. 72 (1980) 6332, https://doi.org/10.1063/1.439156.
[43] J.G. McCarty, H. Wise, J. Chem. Phys. 74 (1981) 5877, https://doi.org/10.1063/1.440905.
[44] J.G. McCarty, H. Wise, J. Chem. Phys. 76 (1982) 1162, https://doi.org/10.1063/1.443085.
[45] J.G. McCarty, K.M. Sancier, H. Wise, J. Catal. 82 (1983) 92, https://doi.org/10.1016/0021-9517(83)90120-3.
[46] J.G. McCarty, H. Wise, J. Catal. 94 (1985) 543, https://doi.org/10.1016/0021-9517(85)90218-0.
[47] G. Berhault, M. Lacroix, M. Breysse, F. Mauge, J.-C. Lavalley, H. Nie, L. Qu, J. Catal. 178 (1998) 555, https://doi.org/10.1006/jcat.1998.2196.
[48] G. Berhault, M. Lacroix, M. Breysse, F. Mauge, J.-C. Lavalley, L. Qu, J. Catal. 170 (1997) 37, https://doi.org/10.1006/jcat.1997.1733.
[49] M. García-Diéguez, D.D. Hibbitts, E. Iglesia, J. Phys. Chem. C 123 (2019) 8447, https://doi.org/10.1021/acs.jpcc.8b10877.
[50] M. García-Diéguez, E. Iglesia, unpublished results.
[51] E.I. Gürbüz, D.D. Hibbitts, E. Iglesia, J. Am. Chem. Soc. 137 (2015) 11984, https://doi.org/10.1021/jacs.5b05361.
[52] C.H. Bartholomew, P.K. Agrawal, J.R. Katzer, Adv. Catal. 31 (1982) 135, https://doi.org/10.1016/S0360-0564(08)60454-X.
[53] D.R. Alfonso, Surf. Sci. 602 (2008) 2758, https://doi.org/10.1016/j.susc.2008.07.001.
[54] D.R. Alfonso, J. Phys. Chem. C 115 (2011) 17077, https://doi.org/10.1021/jp2048426.